Review Article

Peculiar Size Effects in Nanoscaled Systems

M. Maaza[1,2]
https://orcid.org/0000-0002-3820-7838
Maazam@unisa.ac.za
Maaza@tlabs.ac.za

M. Henini[1,2,3]
https://orcid.org/0000-0001-9414-8492

F. Ezema[1,2,4]
https://orcid.org/0000-0002-4633-1417

E. Manikandan[1,2,5]
https://orcid.org/0000-0002-3307-5776

J. Kennedy[1,2,6]
https://orcid.org/0000-0002-1128-987X

K. Bouziane[1,2,,7]
https://orcid.org/0000-0001-6924-2495

M. Chaker[1,2,8]
https://orcid.org/0000-0001-9781-8842

A. Gibaud[1,2,9]
https://orcid.org/0000-0002-7777-6427

A. K. F. Haque[1,2,10]
https://orcid.org/0000-0002-1735-3967

Z. Nuru[1,2,11]
https://orcid.org/0000-0001-7240-642X

I. Ahmad[1,2,12]
https://orcid.org/0000-0002-2905-880X

R. Obodo[1,2,4]
https://orcid.org/0000-0001-7418-8526

M. Akbari[1,2]
https://orcid.org/0000-0003-4220-7221

1 UNESCO–Unisa Africa Chair in Nanoscience and Nanotechnology, College of Graduate Studies, University of South Africa.
2 Nanosciences African Network, iThemba Labs, National Research Foundation, South Africa.
3 School of Physics and Astronomy, University of Nottingham, United-Kingdom.
4 Department of Physics, University of Nigeria.
5 Physics Department, Thiruvalluvar University, India.
6 National Isotope Centre, GNS Science, New Zealand.
7 International University of Rabat, Morocco.
8 National Institute for Scientific Research, Energy and Materials, Canada.
9 Le Mans University, France.
10 Department of Physics, University of Rajshahi, Bangladesh.
11 Department of Physics, Adigrat University, Ethiopia.
12 National Centre for Physics, Pakistan.

Nano-Horizons
https://www.scienceopen.com/collection/NanoHorizons https://doi.org/10.25159/NanoHorizons.9d53e2220e31
Volume 1 | 2022 | 36 pages

Abstract

In this minireview, we intend to shed light on relatively recent examples related to the size and shape effects on materials at the nanoscale and their usage to test a set of quantum mechanics governed phenomena.

Keywords: nanoscale; nanomaterials; size effects; surface effects; surface coordination; quantum confinement; electrons or phonons confinement; surface-to-volume ratio

1 Introduction

Notwithstanding their specific characteristics in general, nanomaterials have ushered in broad applications in a variety of fields [1]. Likewise, they have induced an unprecedented synergy at the interface of various disciplines. The diminutive word "nano" was first used in 1914 by Adolf Zsigmondy [2], then coined by Norio Taniguchi [3], and popularized by physicist Richard Feynman in his famous lecture of 1959 titled "There's plenty of room at the bottom" [4]. From a historical viewpoint, it is exemplified by the Lycurgus Cup from the Roman era, which contained nanoscaled gold embedded in glass exhibiting different colours related to the nanoscaled Au's plasmonic selective absorptions. However, it was Faraday, in the mid-1850s, who established scientifically nano-Au synthesis. Among the specific fingerprints of the nanoscaled materials are size effects, electrons or phonons confinement, and the breaking of the 3D symmetry, including an elevated surface-to-volume ratio [5]–[10].

As schematically represented in Figure 1(a), the surface atoms experience a 3D broken crystallographic symmetry; surface effects and surface tension phenomena are therefore the prime driving forces of phase stabilisation and/or phase transitions, if any [6]–[8]. In addition, the vibrational modes of the external surface atoms are likely to be altered relative to those in volume. Consequentially, the phonons' behaviour would be affected with even a significant phonons confinement [9]. Likewise, free electrons would experience spatial confinement in such quantum wells owing to limited space, inducing quantised energy states and/or tunable bandgaps [10]. Equally important if not paramount in several technological applications of nanoscaled materials is their surface-to-volume (S/V) ratio as schematically represented in Figure 1(b). In general, nanosystems, with one of their dimensions ≤ 100 nm, can be engineered in various configurations such as independent nanoparticles with an isotropic or anisotropic shape (1-D) and 2-D systems (sheets) or thin films as well as multilayered systems or their nanocomposites (Figure 1(c)). In this minireview, we intend to exemplify the rich field of size effects in nanoscaled materials via a set of examples in optoelectronics, photonics, condensed matter, and solid-state and quantum mechanics. More precisely, the following examples are treated:

- size effect and photoluminescence tunability in nanoscaled ZnO;
- size effect and melting temperature in nanoscaled NaCl;

- size effect and phonons confinement in nanoscaled TiO_2;
- size effect and phase transition in nanoscaled Hg;
- shape effect and Anderson localisation in carbon nanotubes (CNTs); and
- nanoscale and quantum mechanical behaviour of neutrons, neutron trapping and neutron lifetime.

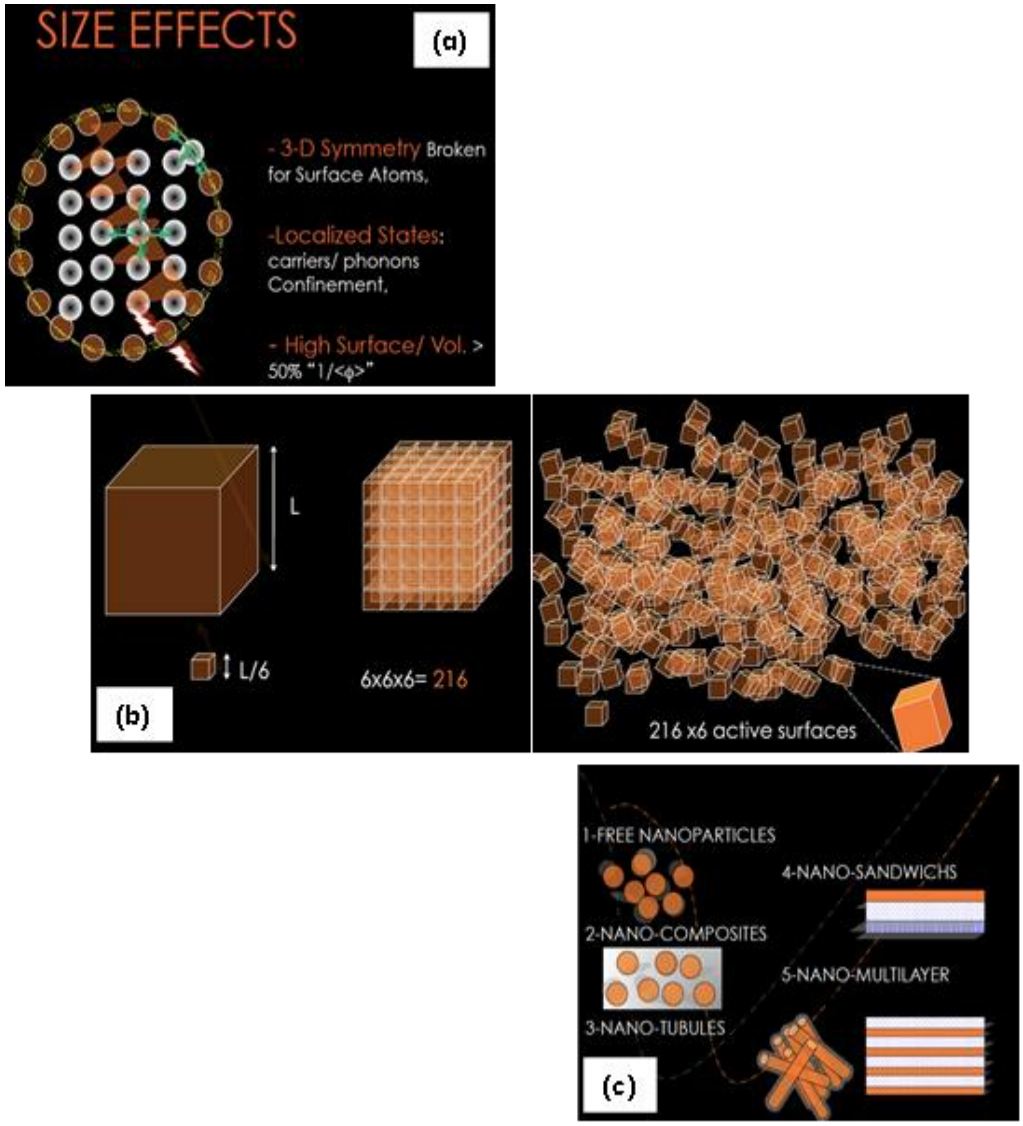

Figure 1: Major size effects induce (a) the breaking of the 3D symmetry, electronic and phonons' confinement
(b) the enhanced S/V
(c) various configurations of nanoparticles

2 Size Effect and Intrinsic Luminescence Tunability in ZnO

Among the family of the so-called transparent conducting oxides (TCOs), ZnO and its doped compounds are the most investigated nanoscaled optoelectronic system so far. ZnO is a wide direct band-gap semiconductor (Eg = 3.7 eV) with a substantially high excitonic binding energy of 60 meV. It crystallises in the wurtzite crystallographic structure while exhibiting optical properties similar to those of GaN. However, compared to this, ZnO has a superior advantage. It is significantly stable with a melting temperature as high as 2 248 K, withstanding therefore high-temperature treatments associated with doping and forming ohmic contacts [11]. Yet, ZnO has been synthesised with various shapes; its wurtzite-related facets, especially those of ZnO hexagon-shaped particles, were shown to play a unique role in its photonics properties. When Fabry-Pérot lasing individual cavities, a lasing effect was reported in spatially oriented ZnO nanowires with an average diameter of about 60 nm [12] and in nanoplatelets [12]–[13]. Correlated to such a lasing effect is its intrinsic excitonic ultraviolet emission. This manifests itself with an emission peak within the spectral UV-blue range of 380–390 nm. This section reports on the size effect exhibited by ZnO nanodiscs on their room temperature (RT) intrinsic excitonic emission [14].

Figure 2(a) displays a scanning electron microscopy of freeze-dried synthesised ZnO nanodiscs with a constant average diameter $< Ø >$ and a variable basal thickness $< D >$ [14]. While the average diameter of the nanodiscs was kept constant at about $< Ø > \sim 7$ nm, their average transversal thickness varied within the range of 9–42 nm. More precisely, $< D >$ was fixed to ~ 9.3, 15.8, 27.2, and 41.7 nm by favouring the growth of the ZnO nanodiscs within the transversal direction (c-axis). Figure 2(b) displays a typical XRD profile of such nanodiscs. ZnO, a typical member of the wurtzite family, crystallises preferentially within the "c-axis" as the easy growth direction. As a result, the three fastest growth directions are $< 0001 >$, $< 0110 >$, and $< 2110 >$, and the polar surface-induced phenomena [15]. The current nanodisc shape (Figure 2(a)) substantiates such a preferred growth direction via the constancy and the variation of $< Ø >$ and $< D >$, respectively. It is therefore worth investigating the size effect on the nanodiscs' excitonic ultraviolet emission versus their thickness $< D >$, if any. Because of its intrinsic emission, ZnO has been receiving worldwide attention for its potential application in solid-state lighting devices such as light-emitting and laser diodes [16]–[20].

Figure 2(c) displays the RT of the nanodiscs' excitonic emission for the various samples under an external UV excitation of $\lambda_{exc} = 337.1$ nm. As one can notice, there is a net size dependence versus the nanodiscs' thickness $< D > \sim 9.3$, 15.8, 27.2, and 41.7 nm. More precisely, there is a significant blue shift of the maximum of the excitonic emission λ_{em}^{max} with the thickness $< D >$; Smaller is $< D >$, smaller is λ_{em}^{max}, and therefore higher is the corresponding excitonic energy Excitonic. This latter parameter, Excitonic, is therefore size-dependent. It is = 3.22, 3.20, 3.17, and 3.11 eV for $< D > \sim 9.3$, 15.8, 27.2 and 41.7 nm, respectively. Figure 2(d) reports such a size

dependence which seems to indicate a likely linear variation of the spectral position of the excitonic emission Excitonic versus 1/< D >. Such a size dependence is in line with several reported experimental observations [21]–[23].

The second parameter deserving investigation is the potential size variation of the width at half maximum of this excitonic emission $\Delta\lambda_{1/2}$. Figure 2(e) depicts the width at half maximum of the Excitonic emission peak. As one can notice, small < D > gives rise to a small full width at half maximum of the excitonic peak value, ie narrowing the excitonic peak. If the size evolution of the excitonic peak's spectral position is as expected and in an agreement with the standard experimental literature, the variation of the full width at half maximum of the excitonic peak versus < D > as reported in Figure 2(e) is certainly not in regard of size-induced quantum confinement effects. In light of such, one should underline that it is well established that the size dependence excitonic shift and its broadening in various ZnO nanoscaled systems could be due to mainly four effects, namely, (i) quantum confinement [23], [24]–[30], (ii) defects density and size-dependent charge carrier dynamics in the ZnO nanoparticles [31]–[38], (iii) shape effect [15], [23], [39]–[41], and (iv) surface strain/stress and surface phenomena [42]–[45].

In summary, several size-dependent variations were observed in the photoluminescence properties of ZnO nanodiscs versus their basal thickness < D >: (i) the excitonic peak's spectral position is basal size-dependent; the maximum of the excitonic emission lmax shifts to low values when the ZnO nanodiscs' thickness < D > decreases ($\lambda^{max} \sim$ < D >), and (ii) the excitonic peak's width at half maximum $\Delta\lambda_{1/2}$ is basal size-dependent; it becomes sharp when the ZnO nanodiscs' thickness < D > decreases ($\Delta\lambda_{1/2} \sim 1/$< D >).

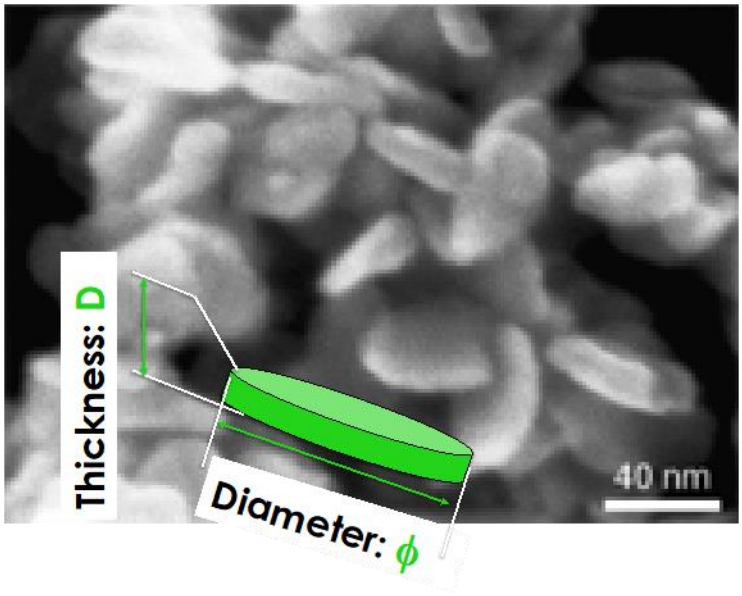

(a)

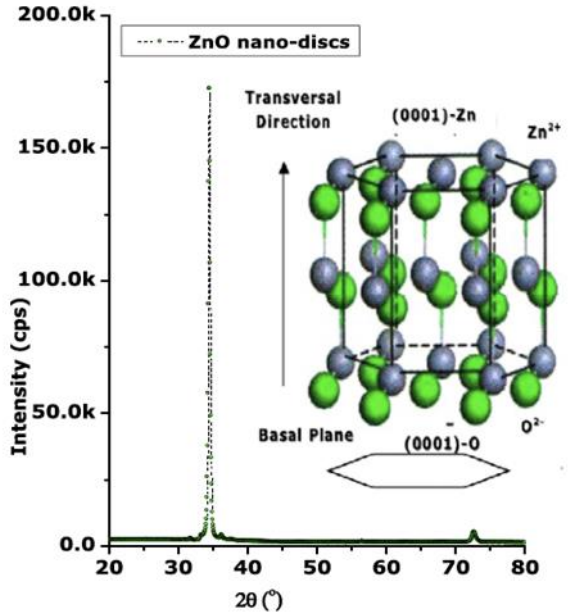
ZnO nano-discs
Intensity (cps)
200.0k
150.0k
100.0k
50.0k
0.0
20
30
40
50
60
70
80
2θ (°)
Transversal Direction
(0001)-Zn
Zn2+
O2-
Basal Plane
(0001)-O

(b)

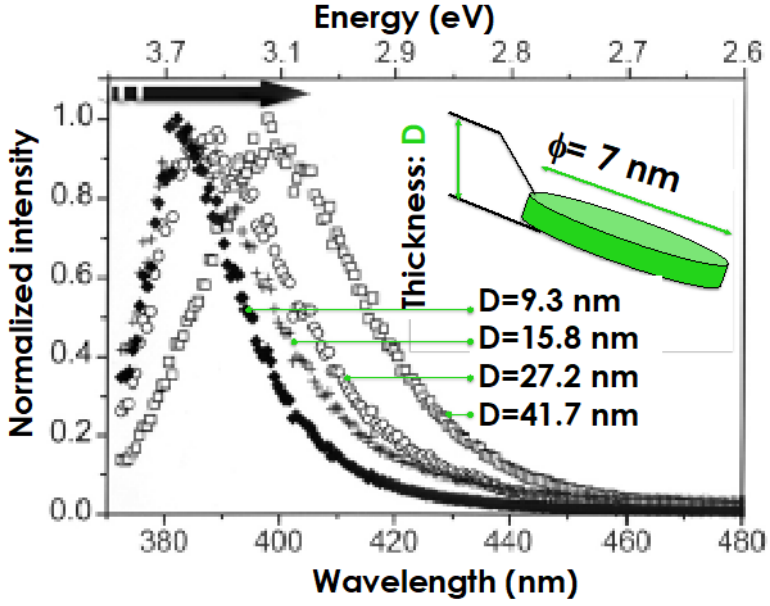
Energy (eV)
3.7
3.1
2.9
2.8
2.7
2.6
Normalized intensity
1.0
0.8
0.6
0.4
0.2
0.0
380
400
420
440
460
480
Wavelength (nm)
Thickness: D
ϕ= 7 nm
D=9.3 nm
D=15.8 nm
D=27.2 nm
D=41.7 nm

(c)

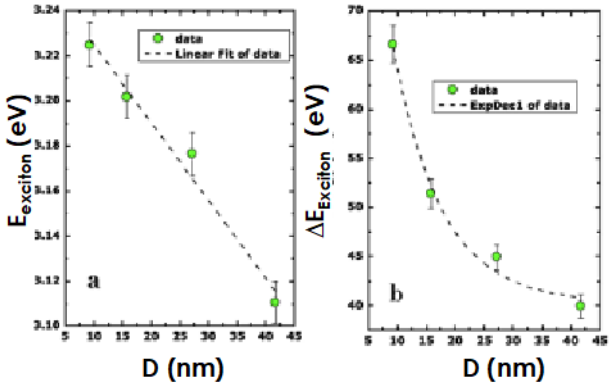

(d) (e)

Figure 2: (a): Scanning electron microscopy of freeze-dried ZnO nanodiscs exhibiting a nearly constant diameter Ø and variable thickness D
(b): Their corresponding X-ray diffraction pattern showing a preferential growth direction within the wurtzite crystallographic structure
(c): Intrinsic photoluminescence emissions of the various ZnO nanodiscs with different thicknesses (D = 9.3, 15.8, 27.2 and 41.7 nm)
(d): Band-gap evolution versus D
(e): Thickness width at half maximum evolution versus D

3 Size Effect and Melting Temperature of NaCl Nanocrystals

Because of the high S/V ratio and the breaking of the 3D symmetry, the thermodynamic properties of nanomaterials such as the melting, vaporisation and/or sublimation temperatures are governed by surface effects in general, and surface atomic coordination as genuinely demonstrated in the classical case of gold nanoparticles by Buffat and Borel [46] and in the case of nanoscaled sodium chloride (NaCl) by Kana *et al*. [47]. In bulk form, NaCl has a cubic unit cell with a face-centred cubic lattice type and space group (Fm3m) with a cell lattice parameter < a > = 5.6410 Å. Its bulk thermodynamic melting and vaporisation temperatures are 1 074.5 and 1 686 K, respectively. Its bulk modulus and specific heat capacity are of the order of 24.42 GPa and 854 JK^{-1}, respectively. In its nanosised form, NaCl nanocrystals should exhibit a lower surface cohesive energy owing to the large ratio of surface ions, leading to a significant reduction of the ionic bonds. This breakdown of the 3D symmetry at the surface would likely enhance the surface reactivity of the NaCl nanocrystals. The macroscopic parameters, such as the melting and/or sublimation point, would therefore be size-dependent as predicted theoretically for numerous metallic and semiconducting materials [48]–[49].

Similarly, owing to the additional surface tension effects, NaCl nanocrystals could exhibit a lower symmetry crystallographic structure. With the intention of investigating possible size effects in NaCl, specifically and related halides in general, one should

consent to consider the electric polarisability of the Na^+ Cl^- surface pairs as well as their surface vibrational modes. At first glance, if one considers that the surface $Na^+ - Cl^-$ pairs act as independent molecules, their cohesive energy is equivalent to free $Na^+ - C^-$ molecules, ie of ~ –74 kcal/mole, while the in volume $Na^+ - Cl^-$ molecules are affected by the Madelung electrical crystal field. Their corresponding cohesive energy is therefore bulk related, ie ~ –152 kcal/mole. Accordingly, the higher is the S/V ratio and the smaller is the melt/sublimation energies. These size effects have been estimated theoretically on the basis of the semi-infinite continuum model. More accurately, semi-infinite lattice dynamic calculations and molecular-lattice dynamics [50]–[52] early investigations on size effect on the enhancement of specific enhancement in NaCl powder have been performed by Patterson *et al*. [53]. This theoretical study has revealed an enhancement of the specific heat capacity several times larger than predicted with the semi-infinite model [54]–[60]. This section presents size effects in the melting/sublimation of NaCl nanocrystals.

Figure 3(a) displays the transmission electron microscopy (TEM) of freeze-dried NaCl nanoparticles [47] investigated to shed light on the size dependence of their melting/sublimation temperature, if any. The nanocrystals are cuboidal in shape with a transversal dimension D_{Trans} = 63.5, 75.2, 91.7 and 108.3 nm corresponding to basal dimension L_{Basal} of 0.4–0.9, 0.7–1.2, 0.9–1.5 and 1.3–1.7 μm, respectively. Figure 3(b) displays the RT X-ray diffraction pattern of the micrometric, as well as the nanometric NaCl samples, pressed powders corresponding to bulk NaCl and NaCl nanocrystals with the lowest D_{Trans} and L_{Basal} values (D_{Trans} = 63.5, L_{Basal} = 0.4–0.9 μm) in the angular range of 26° to 47° especially. As one can notice, besides the slight difference in the Bragg peaks' intensity, the crystallographic and texturing of the NaCl nanocrystals are quasi-similar to bulk but with a noticeable angular shift. These significant angular shifts of the ⟨110⟩, ⟨200⟩ and ⟨220⟩ Bragg peaks of the NaCl nanocrystals are compatible with an extensive surface pressure inducing a noteworthy ⟨110⟩, ⟨200⟩ and ⟨220⟩ reticular planes expansion $\langle \Delta d_{hkl} \rangle / \langle d_{hkl} \rangle$. Figure 3(c) displays the variation of the deduced lattice parameter $\langle a \rangle = \langle d_{hkl} \rangle / (h^2 + k^2 + l^2)^{1/2}$ derived for most intense Bragg peaks. The average value ⟨a⟩ is about 5.6280 and 5.6410 Å for bulk and nanosized NaCl crystals, respectively. The corresponding relative volume expansion of the elementary cell of the NaCl nanocrystals is therefore of the order of $\Delta V/V$ = 0.7%. For such a halide material, such a non-negligible value could be correlated to the intrinsic softness of NaCl itself. If one considers that the bulk modulus B_{Bulk}^{NaCl} = 2.442010 N/m^2 [59] is alike at the nanoscale, the surface pressure on the nanosized NaCl nanocrystals is of the order of $P \sim K\, \Delta V/V \sim 0.17$ GPa.

Figure 3(d) displays the thermogravimetric mass loss versus temperature of the NaCl nanocrystals (D_{Trans} = 63.5 nm) and its bulk equivalent. There is a net difference in the behaviour of the two curves as low as 100°C. Indeed as shown by the inset zoom displaying the mass loss within the temperature range 0–300ºC of the bulk and those corresponding to nanocrystals with D_{Trans} = 63.5 and 75.2 nm. In these latter cases, the sublimation of the NaCl nanocrystals seems to deviate from the standard linear

melting/sublimation process but rather goes through various stages while being size-dependent [60].

The smallest nanocrystals of NaCl with D_{Trans} = 63.5 nm start sublimating below 323.5 K. Figure 3(e) displays the sublimation temperature of the NaCl nanocrystals versus the normalised $D_{Trans}/D_{Trans}^{max}$. At first glance, the sublimation/vaporisation temperature T_{sub} seems to vary as $T_{sub} = \alpha (D_{Trans}/ D_{Trans}^{max})^2$. In summary, several size-dependent variations such as the following were observed in the melting properties of NaCl nanocrystals versus their transversal thickness < D_{Trans} >:

- the sublimation temperature is size-dependent as T_{sub} α $(D_{Trans})^2$; and
- the smallest nanocrystals of NaCl with D_{Trans} = 63.5 nm start sublimating below 323.5 K, far below the bulk value of 1 686 K.

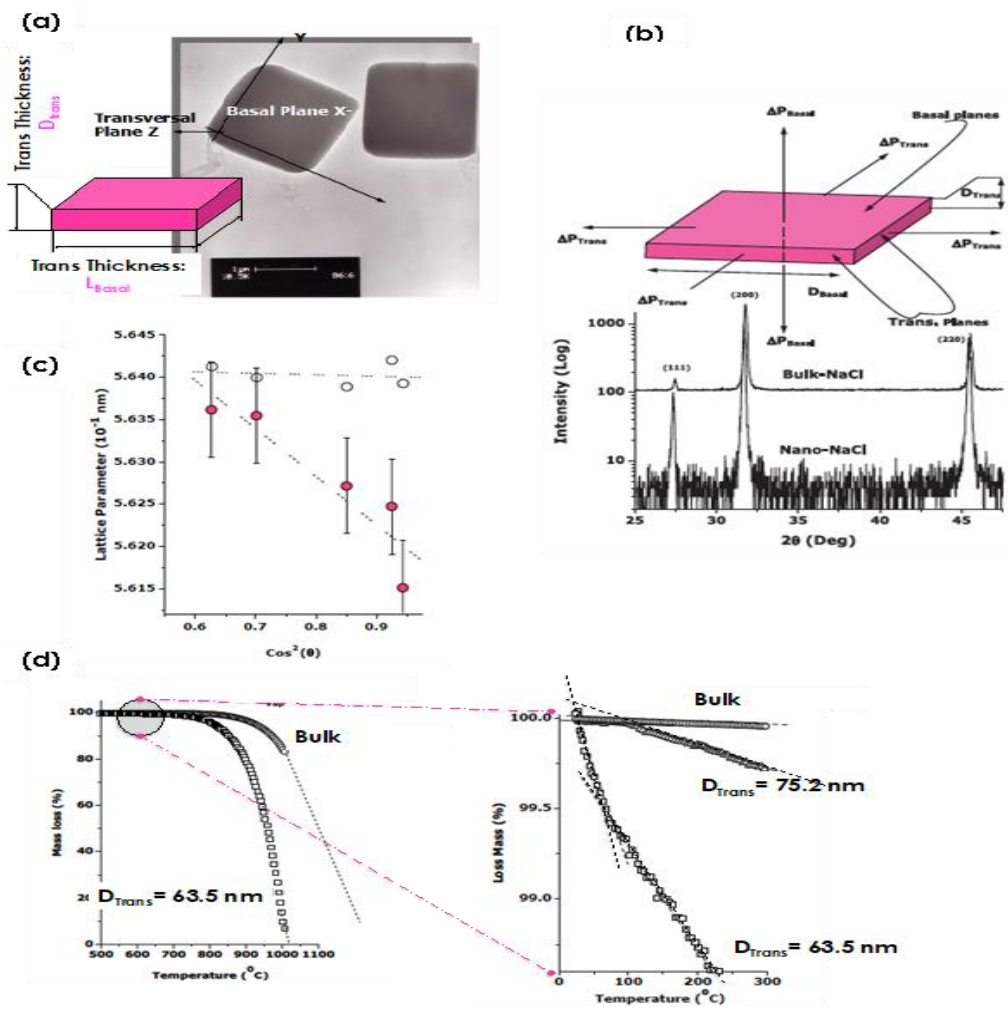

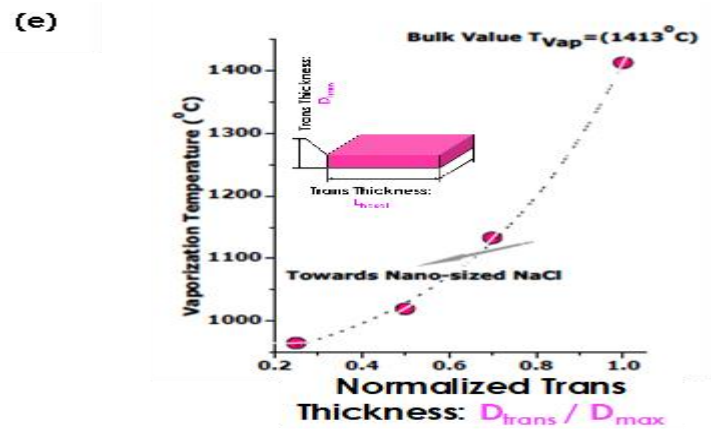

Figure 3: (a): Scanning electron microscopy scan of freeze-dried NaCl nanoplatelets exhibiting a variable transversal thickness D_{Trans}
(b): X-ray diffraction spectra of bulk and nanocrystalline NaCl and its corresponding strain/stress
(d): Thermogravimetry mass loss of bulk and nanocrystalline NaCl. The inset indicates a significant deviation of the melting/sublimation at the nano relatively to bulk
(e): Size dependence of the sublimation/vaporisation of the freeze-dried NaCl nanoplatelets

4 Size Effect and Phonon Confinement in Nanoscaled TiO_2

Owing to the enhanced S/V ratio characterising nanoscaled particles, their surface atoms population suffers a 3D symmetry breakdown, and therefore their atomic vibrational modes will be affected significantly. This would be reflected in the phonons' signature, which should be size-dependent, as observed in Raman spectra in various nanosystems [61]–[70]. More precisely, the Raman active modes exhibit not only a frequency shift but also a significant broadening.

Such a trend was explained considering the breakdown of the phonon momentum selection rule q'0, specific to Raman scattering in ordered systems. In the case of nanocrystals, this rule is no longer valid as the phonons are confined in a defined space, and all the phonons over the Brillouin zone will contribute to the first-order Raman spectra. The weight of the off-centre phonons increases as the crystal size decreases, therefore the phonon dispersion causes an asymmetrical broadening and a shift of the Raman peaks' position [63]–[68]. The Raman intensity over the Brillouin zone was found to be size-dependent as [61]–[62]:

$$I(\omega) = \int \exp(-q^2 Ø^2/16\pi^2)\, d^3q/[(\omega-\omega(q))^2 + (\Gamma_0/2)^2]$$

where Γ_0 is the Raman linewidth at RT, and Ø is the average size of the nanoparticles.

The broadening and the shift of the Raman peak are a result of this integration. This model has successfully described various Raman size-dependent trends in several nanoscaled materials, including; Si, ZnO and TiO_2. This latter oxide is of particular interest. It possesses a rich family of polymorphs in addition to the major phases of anatase, rutile and brookite crystallographic phases, as shown in Figure 4(a). The anatase form is the most investigated phase in view of its physical–chemical properties in line with several technological applications, including their unique photocatalytic response. From a vibrational point, anatase exhibits six vibrational modes ($A1g_12B1g_13Eg$), with the most intense one, Eg, spectrally located at the vicinity of 144 cm^{-1}.

Figure 4(c) displays the principal Eg mode of anatase TiO^2 nanoparticles synthesised by freeze-drying (Figure 4(b)) of three different average sizes; Ø = 7, 12 and 62 nm. As one can notice, both the width at half maximum $\Delta\omega_{1/2}$ and the spectral position of the principal Eg mode ω_{max} are size-dependent. $\Delta\omega_{1/2}$ was found to be 12.3, 8.1 and 7.2 cm^{-1} for Ø = 7, 12 and 62 nm, respectively. ω_{max} was found to be 150.5, 147.3 144.3 cm^{-1} for Ø = 7, 12 and 62 nm, respectively. Hence smaller is the TiO_2 nanoparticles' size Ø, broader is the mode, and higher is its Raman shift.

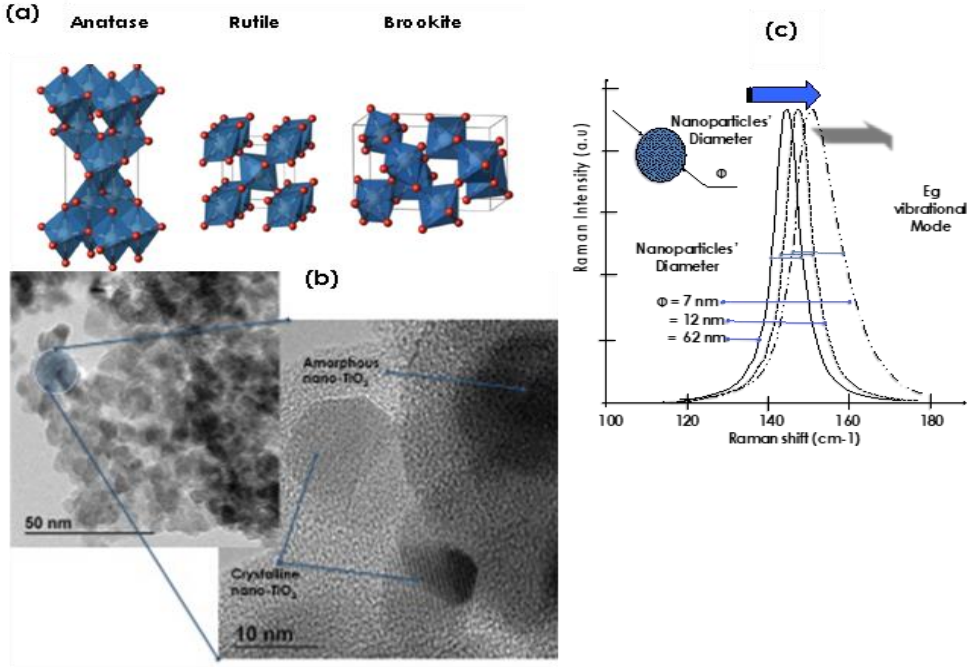

Figure 4: (a): Major RT stable phases of TiO2, anatase, rutile and brookite
(b): TEM images of anatase nanoparticles
(c): Raman spectra of the Eg vibrational mode of the various nano-TiO_2 with diameter Ø ~ 7, 12 and 62 nm

5 Size Effect and Phase Transition in Nanoscaled Hg

As mentioned previously, the elevated S/V ratio in nanoscaled materials substantially affects the coordination of the surface atoms as well as their short and mid-range atomic ordering. Surface tension and related properties therefore become pre-eminent and would significantly affect any phase transition phenomena such as crystallographic phase transitions, including solid-solid and potentially liquid-solid transitions [71]. This section intends to exemplify the size effect on the liquid to the solid phase transition of nanoscaled mercury (Hg).

Hg has the highest RT elemental surface tension; g ~ 486 mN/m [72]. Accordingly, the theoretical calculations were made on the liquid-vapour interface of simple metals in general [73]–[74]. Approaches based on the jellium model [75] and the perturbation expansion up to the second order in the surface "e-ion" pseudo-potential [76]–[77] indicated that excessive surface tension could stimulate a significant surface atomic layering of three to five atomic planes (as depicted in Figure 5(a)) and their related periodic S/V electron density distribution. This surface atomic ordering, in full agreement with the capillary wave theory, has been observed by X-ray reflectivity measurements on a bulk liquid mercury surface [78]. Likewise, Bafile *et al*. [79]–[80] showed that such an atomic ordering could be segregated in the bulk liquid mercury by examining the height and the width in addition to the position of the main peaks of the static structure factor S(Q) at ambient conditions. Both X-rays and neutron diffraction S(Q) profiles revealed a structure of up to four or five discernible peaks: a feature of a local surface atomic ordering [80].

Such a surface atomic ordering at RT observed on the flat surface of bulk Hg could be enhanced significantly if not drastically on nano-Hg particles if one could engineer them. Indeed, owing to their substantial S/V ratio and the 3D symmetry breakdown, the surface atoms population would be greater in nanoscaled Hg. Henceforth, at such a scale, the surface phenomena dominate gravity effects in view of the significantly elevated surface tension of Hg (Figure 5(b)). If engineered, the enhanced surface ratio of nano-Hg of radius "Ønano-Hg/2" should induce an excess of Laplace surface pressure $\Delta P \approx 4\gamma/Ø_{nano\text{-}Hg}$ of tens of MPa. As a simple estimation, if $Ø_{nano\text{-}Hg} \approx 2.50$ nm, $\Delta P \approx 0.76$ GPa at RT. Considering the mercury phase diagram of Figure 5(c), such an excess surface pressure of 0.76 GPa should induce at RT a net crystallisation out of the liquidus space to the solid α-rhombohedric phase [81]–[83] of the nano-Hg (Figure 5(c)). This atomic ordering phenomenon at RT should therefore manifest itself through a significant crystallisation of the liquid phase to the solid rhombohedral "α-type" phase at RT via a standard X-ray diffraction technique, only if it would be possible to synthesise Hg nanoparticles with an average diameter $Ø_{nano\text{-}Hg} \approx 2.50$ nm or less. If so, Hg would become solid at RT. But, if synthesised independently, the nanoparticle of Hg would coalesce promptly. It is therefore necessary to trap them in a chemically inert host matrix, as schematically represented in Figure 5(d).

Figure 5(e) displays a TEM of the nanoscaled Hg particles embedded in a chemically inert boron nitride (BN) host matrix. As pointed out previously, this approach was required to ensure that the BN would act effectively as a barrier to avoid the coalescence of the Hg nanoparticles. As one could notice in the TEM of Figure 5(f), the Hg nanoparticles are almost quasi-spherical in shape with substantially truncated interfaces. The diameter of the Hg nanoparticles ranges from 1.5 to 28.9 nm for the Hg-BN nanocomposite (Figure 5(g)). Few larger distorted Hg nanoparticles of ~63–70 nm in diameter are observed too. This could be congruent with sample zones exposed to noteworthy heat from the TEM probing e-beam. Figure 5(h) displays the X-ray diffraction pattern of the Hg-BN nanocomposite consisting of nanoscaled Hg particles of $\langle Ø_{\text{nano-Hg}} \rangle_{\text{TEM}} \sim 2.4$ nm dispersed homogeneously in the BN host matrix. More precisely, it displays the diffraction patterns at room temperature (RT = 293.5 K) and nitrogen temperature (78 K), ie below the solidification temperature of bulk Hg ($T_{\text{Hg solidification}} = -38.83$°C, 234.3 K). The RT Hg-BN nanocomposite's pattern exhibits one narrow and two larger diffraction peaks.

The narrow Bragg peak is assigned to the turbostratic BN-t host matrix (121) diffraction "ASTM Card 18-0251" (84). The first intense broad Bragg peak centred at $2\Theta \sim 32.781°$ ($57.18\ 10^{-2}$ rad) with a width at half maximum of $\Delta\Theta \sim 6.30\ 10^{-2}$ rad can only be assigned to crystallised mercury; more precisely to the α-rhombohedric (101) reticular orientation "ASTM Card 09-0253". Yet broad, such a Bragg peak could be considered a signature of a preliminary atomic ordering exhibited mostly by surface mercury atoms within the non-percolated encaged nano-Hg. Using the Debye-Scherrer approximation for this Hg (101) Bragg peak, the average size of the corresponding Hg nanoparticles in accordance with the Scherrer approximation is $\langle Ø\text{nano-Hg} \rangle_{\text{D-S}} \sim 2.44$ nm. Likely, such an atomic-like ordering would originate from the surface atoms of the nano-Hg population and those with a smaller diameter according to the phase diagram of Figure 5(c).

The second additional broad Bragg peak centred at $2\Theta \sim 39.695°$ ($69.24\ 10^{-2}$ rad) with a width at half maximum of $\Delta\Theta \sim 3.580°$ ($6.25\ 10^{-2}$ rad) (Figure 5(i) and zoom inset). Taking into account both its angular position and the relative intensity to the Hg (101) peak and the specific turbostratic structure of the host BN matrix (12), this Bragg peak could only be assigned to the second intense crystalline Hg Bragg peak, ie the Hg (003) crystallographic orientation of the rhombohedric Hg α-phase "ASTM Card 09-0253". To confirm that the indexed Hg (101) and Hg (003) are proper mercury Bragg peaks originating from the atomically ordered nano-Hg embedded in the BN-t host matrix, the RT nano Hg-BN pattern is compared to its profile which was cooled to 78.0 K (Figure 5(i)). The labelled Hg (101) and Hg (003) develop into sharper peaks with a significant angular shift with three new less intense Hg Bragg peaks corresponding to Hg (110), Hg (104) and Hg (113) in addition to the presence of numerous BN turbostratic diffraction peaks. The coexistence of the two Bragg peaks, namely Hg (101) and Hg (003), in the RT diffraction pattern of Hg-BN nanocomposite is therefore the forthright confirmation of the RT crystallisation of the non-percolated nano-Hg

"$\langle \varnothing_{Hg} \rangle_{TEM}$ ~ 2.4 nm" within the BN-t host matrix and is consistent with seven to eight atomic planes ordering (($\langle a \rangle$ ~ 3.005 Å) (83).

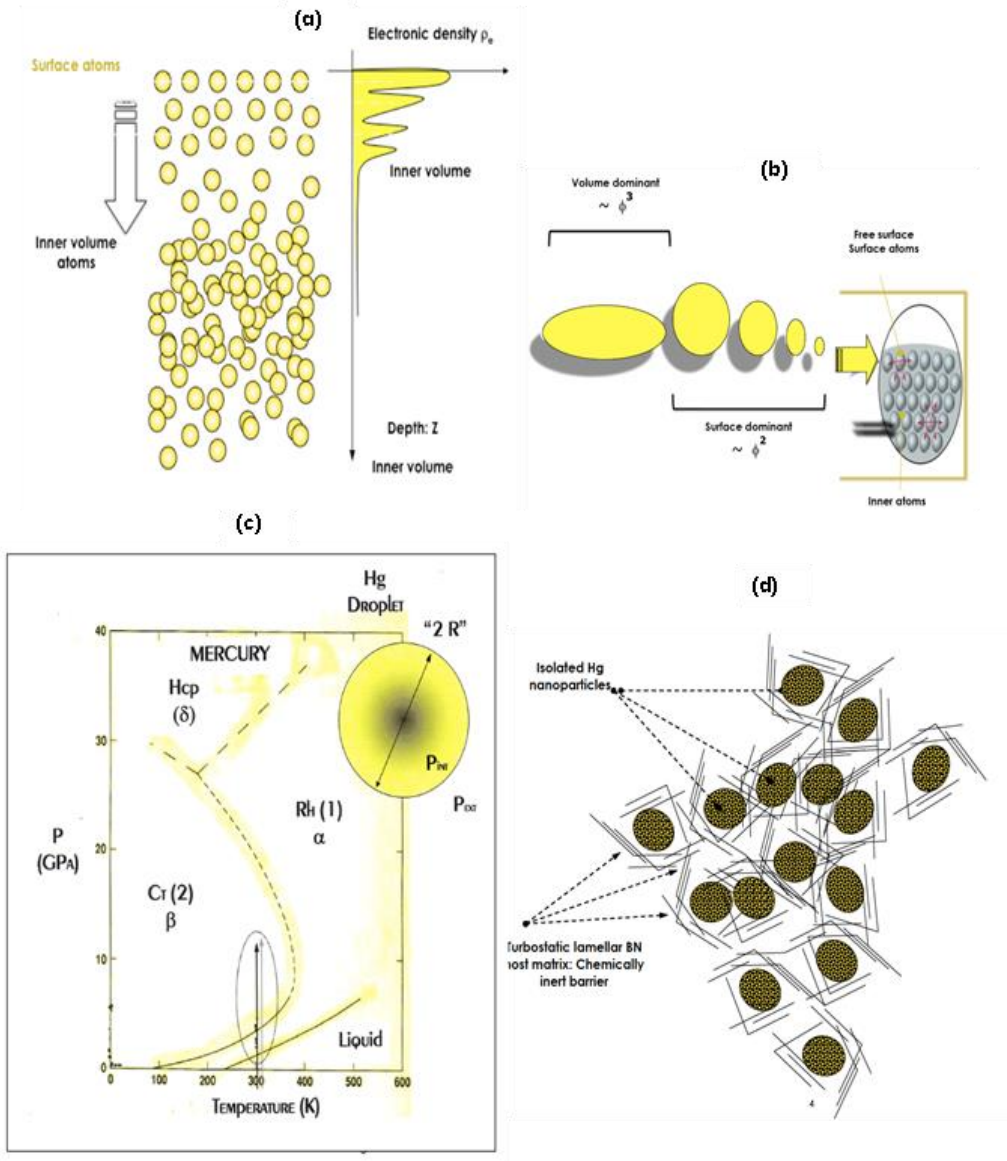

Figure 5: (a): Surface atomic ordering as predicted theoretically and its electronic distribution from surface to inner volume in liquid metals
(b): Volume to surface dominating phenomena in liquid metals
(c): P-T phase diagram of mercury (Hg)
(d): Schematic representation of Hg nanoparticles encaged in turbostratic BN host matrix

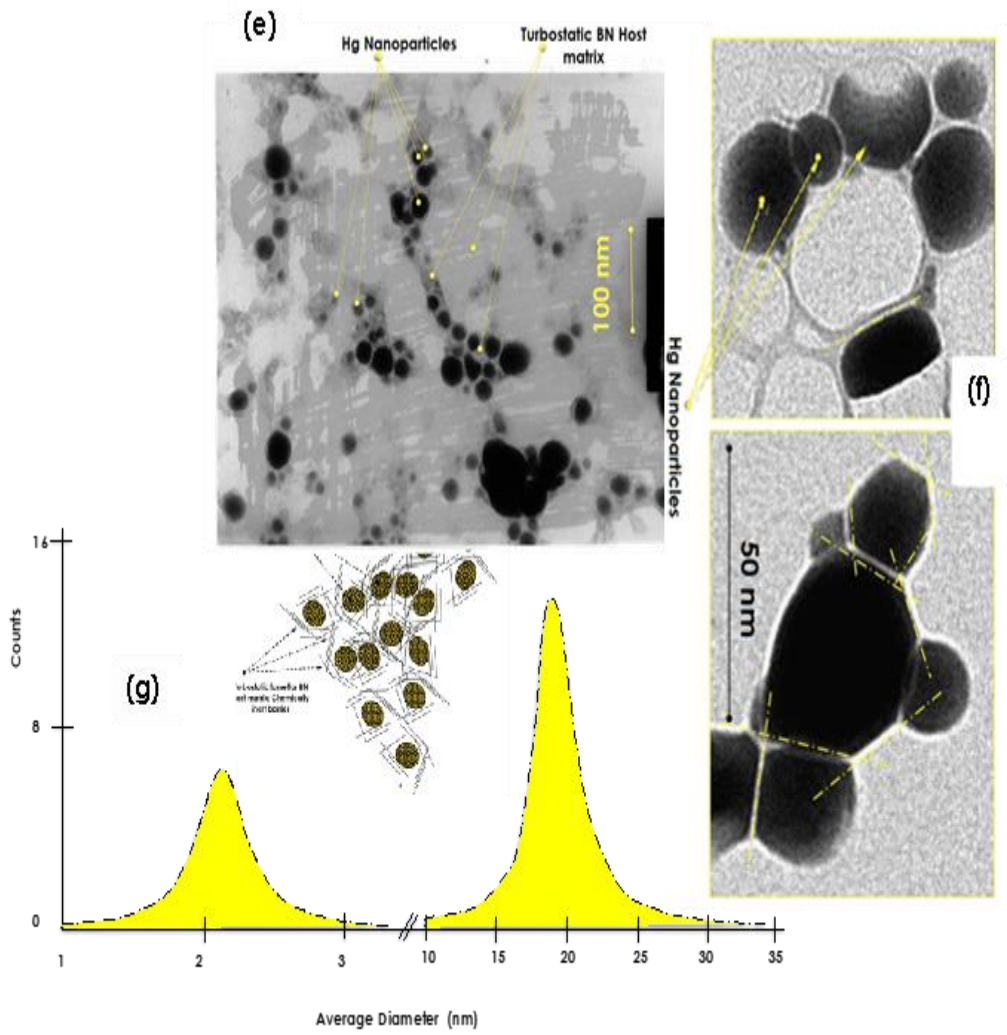

Figure 5: (e): High-resolution TEM image of the Hg1/20-BN sample
(f): High-resolution TEM at higher magnification
(g): Their corresponding size distribution

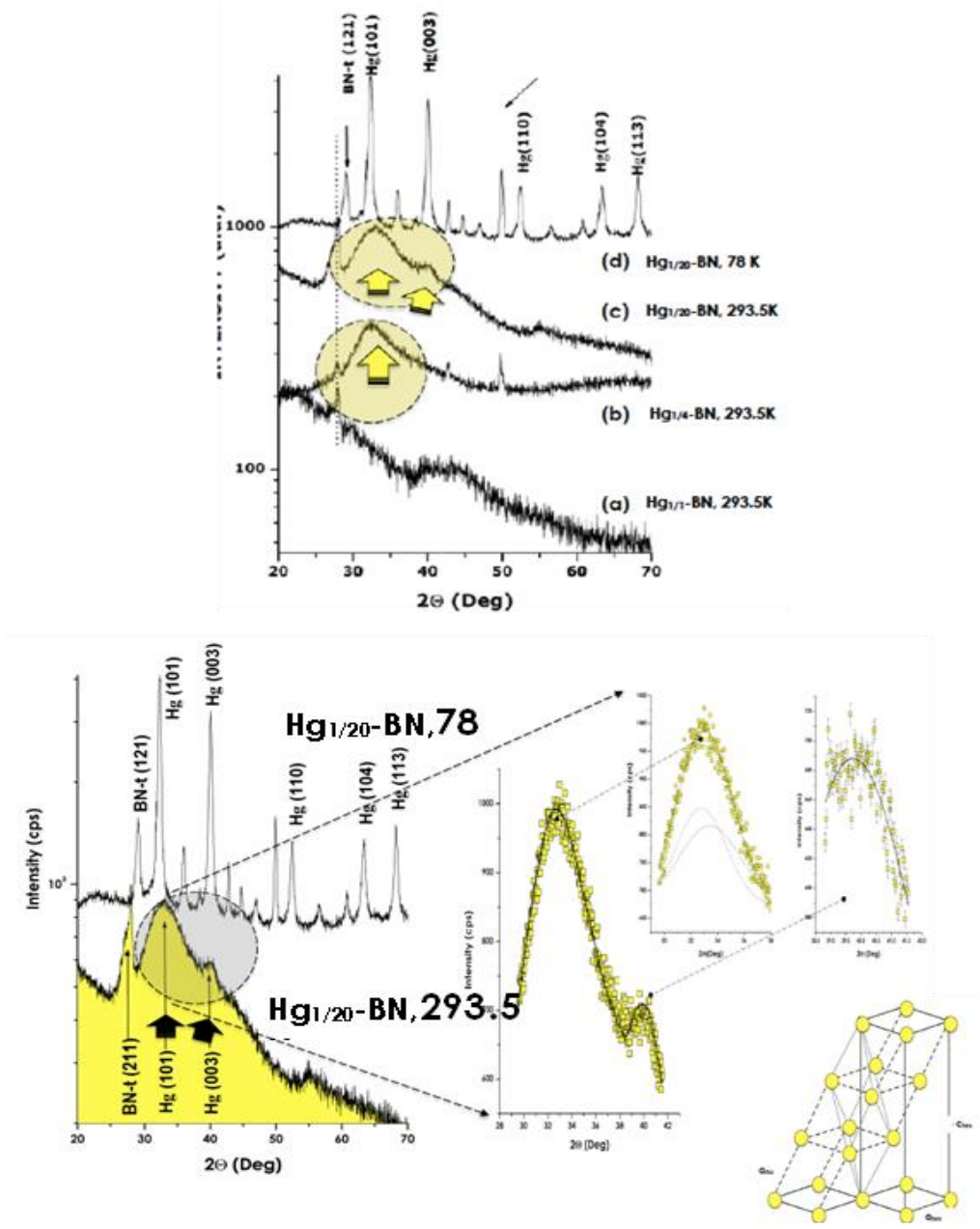

Figure 5: (h): RT X-ray diffraction patterns of the various samples [h-a] Hg1/1BN, [h-b] Hg1/4BN, [h-c] Hg1/20-BN ,[h-d] liquid nitrogen Hg1/20-BN (f)
(i): RT and liquid nitrogen XRD spectra of Hg1/20-BN.The inset reports on the (110) and (003) Hg Bragg peaks

6 Size Effect and Light Quantum Confinement in CNTs

Given their nanoscale dimensions and various shapes, nanoscaled systems are ideal platforms for observing quantum mechanics phenomena at RT, including but not limited to band gap tunability and optical light resonance in disordered conformation [84]–[88]. This subsection presents the case of resonant light scattering in disordered media; more precisely, the Anderson localisation in CNTs.

Within the light scattering configurations, the dominating scattering regimes are the classical Rayleigh and Mie scattering (Figure 6(a)), allowing the determination of the average size of the nanoparticles, their size polydispersity, the nature of their interface and the dynamic of free charge carriers within their confined volume.

In addition to these classical regimes, the so-called Anderson scattering regime [89]–[102] is a quantum-mechanic driven process. Yet, it is complex and generally difficult to observe at RT; it was observed recently in CNTs. This Anderson localisation scattering regime derives from the seminal 1958 Anderson paper titled "Diffusion absence in certain random lattices". Anderson's original focus of this decisive contribution was the investigation of the effect of the disorder on electron transport and/or spin diffusion, specifically in semi-disordered condensed matter. The quantum-mechanic treatment of the electron wave-packets propagation in such disordered condensed matter media exhibited a paradoxical localisation in specific configurations. In view of the wave-particle duality, such a paradoxical localisation can be translated to photons. From the theoretical viewpoint, the Anderson localisation can be summarised in three major configurations [96]–[97], as schematically shown in Figure 6(b): (i) diffusive scattering in a non-absorbing medium; (ii) weak Anderson localisation; and (iii) strong localisation in semi-disordered media. In fact, in these disordered/semi-disordered media, the transport of light with wavelength "λ" depends mainly on the system's length scales. The pertinent scales are the mean free path "ξ" which is the distance after which the light's propagation direction is randomised, and the sample thickness "D". Hence, and as was mentioned above, three main scattering processes can take place in such a disordered/semi-disordered medium with total transmission "T": (i) diffusive scattering in a non-absorbing medium: $\lambda << \xi << D$, $T \cong \xi << D$, $T \cong \xi / D$; (ii) weak Anderson localisation: $2\pi\xi/\lambda \rightarrow 1$, $T \cong 1/D^2$; and (iii) strong Anderson localisation: $2\pi\xi << \lambda$, $T \cong \exp(-D/D_{loc})$. Considering the wave-particle duality, this so-called Anderson localisation was observed in various systems [99]–[108].

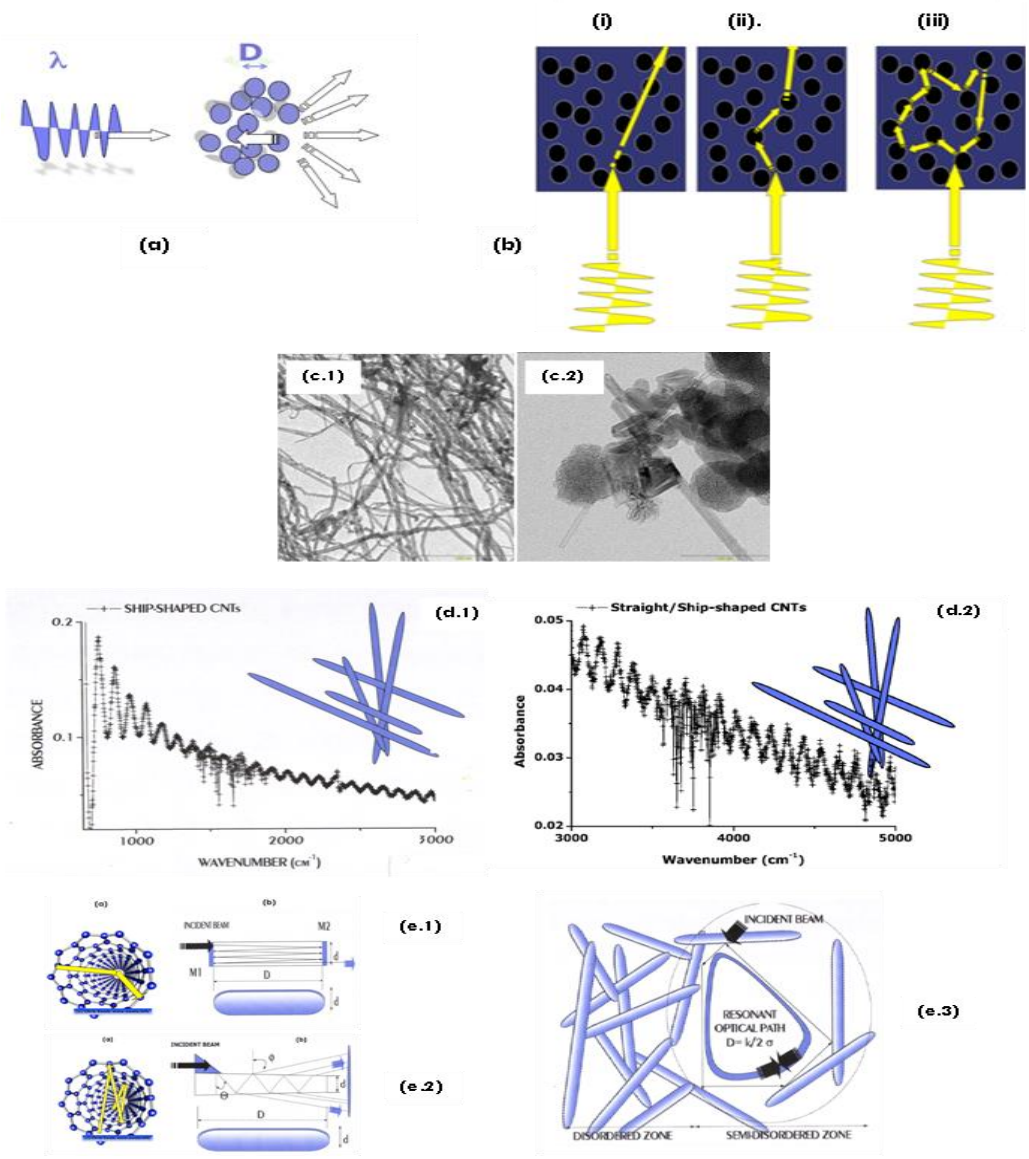

Figure 6: Schematical representation of the (a) standard Mie and Rayleigh scattering (b): Anderson localisation: [b-i] weak localisation, [b-ii] medium localisation, and [b-iii] strong localisation
(c): High-resolution TEM image of spaghetti (c.1) and ship shaped (c.2) CNTs
(d) Interference pattern from attenuated total reflection Fourier transform infrared (IR) spectrometry spectra of the ship-shaped CNT sample (d.1) and (d.2), and potential sources of such an interference pattern
(e): (e.1) Fabry-Pérot resonating cavity, (e.2) Lummer-Gehrcke resonating cavity, (e.3) strong Anderson localisation resonating cavity

CNTs are considered in the current study (Figure 6(c)). The rationale for choosing such a nanosystem lies within the following major motives: (i) individually, CNTs can be highly ordered from a morphological and crystallographic viewpoint, especially if they are highly ordered ship shaped (Figure 6(c.2)) (obtained mainly by pulsed laser vaporisation and not spaghetti type such as those obtained via standard chemical methodologies; (ii) considered a powder, the CNTs distributed isotropically and hence a disordered nanosystem; and (iii) depending on their chirality, the CNTs can be metallic, semiconducting or insulator hence can be highly or weakly IR reflectors. This contribution, as a follow-up to previous work [108], is intended to seek the attention of the photonics community on this challenging Anderson localisation in nanoscaled 1D systems. As mentioned previously, this section is intended to demonstrate the possibility of a strong Anderson localisation of IR light in a 3D system of ship-shaped CNTs.

For such a possibility, and as the ideal investigation technique, the Fourier transform IR under attenuated total reflection geometry (ATR-FTIR) was considered. Figure 6(d) displays the absorbance spectrum of the ship-shaped CNTs in the spectral range of 400–3 000 cm^{-1} (Figure 6(d.1)) and 3 000–5 000 cm^{-1} (Figure 6(d.2)). As one can notice, the spectral absorbance-wavenumber spectra exhibit a rich interferential pattern from 400 up to 5 000 cm-1 with a likely exponential envelope decay. Within such a spectral range, about 40 maxima are counted. These absorbance maxima occur at several sequences of wavenumbers with an average spectral inter-range $\langle \Delta\sigma_{Max} \rangle \approx 105\ cm^{-1}$. As these maxima or absorption enhancements occur at equal wavenumber spacings $\langle \Delta\sigma_{Max} \rangle \approx 105\ cm^{-1}$ that are independent of the specific value of the wavenumber (or frequency), one should conclude that the experimental periodic absorbance profile as generated by a resonating cavity-like of an optical length $n_{cav}\ D_{cav}$ where n_{cav} is the refractive index of the medium filling the resonant cavity of geometrical length (D_{cav}). If so, $n_{cav}\ D_{cav}$ is related to the maxima difference $\Delta\sigma$ via the resonance relation: $\Delta\sigma Max = (2\ n_{cav}\ D_{cav})^{-1}$.

As confirmed previously, such an interference pattern cannot be induced by a transversal interference (Lummer-Gehrcke resonating cavity (Figure 6(e.1)) [111], longitudinal interference (Fabry-Pérot resonating cavity (Figure 6(e.2)) [112] or the resonance of a type of "optical necklace states in localized 1D systems" [113]–[118]. Hence, there is only the possibility of a strong Anderson localisation within the CNTs as schematically represented in Figure 6(e.3), whereby the CNTs act as IR reflectors [108]–[109]. This situation is close to that treated theoretically by Zhu *et al*. [119], whereby they treated the case of internal reflection of diffusive light in disordered media. The exponential decay of the maxima envelops cement furthers the strong Anderson localisation hypothesis [108]–[109].

7 Size Effect and Neutron Quantum Confinement in Nanoresonators

In addition to size and shape effects in nanoscaled materials, nanoresonators can be used to test a variety of quantum mechanics governed phenomena such as trapping neutrons

to estimate their lifetime or test their wave-particle duality. This contribution therefore reports the possibility of trapping free neutrons in nanostructured Fabry-Pérot nanoresonators (Figure 7(a)). The precision of the trapping time of free neutrons in such nanoresonators is governed by the Heisenberg uncertainty and therefore offers, a priori, an attractive precise approach. Yet this concept was proposed by Steyerl *et al*. [120]–[122] with unpolarised beams whereby the trapping approach was observed via dips in the standard neutron total reflection plateau. Such neutron trapping can be validated in various configurations including unpolarised [123]–[124], polarised [125]–[126], isotopic labelling [127]–[128] and/or using notorious highly absorbing materials [129]. In such Fabry-Pérot nanoresonators configuration, the neutron propagation is governed by its quantum mechanics wave-particle duality.

Correlated to such a quantum mechanics wave-particle duality [130], the wave-packet optical behaviour of free neutrons manifests itself through several interference phenomena, including slit diffraction [131], prism deflection [132], edge diffraction [133], diffraction on a ruled grating [129] and interferometry experiments [130]–[131]. It also manifests itself through various interferential-based nanostructures such as multilayered monochromators [132], [136], polarisers [133], [137], interferometers [134]–[135] and supermirrors [138]–[139].

In addition to these climax experiments and neutron optics devices which sustain the quantum mechanics wave-particle duality of free thermal, cold and ultracold neutrons naturally, one can quote the prominent neutron total reflection demonstrated as early as 1946 by Fermi and Zinn [140] and Fermi and Marshall [141]. From an experimental viewpoint, this total reflection phenomenon was used to determine nuclear-bound coherent scattering lengths of different materials [138] and perform non-destructive and advanced surface superconductivity studies [139], [144]. A prominent technological application of this total reflection phenomenon is the transport of neutron beams by multi-reflections to locations quite distant from the research reactor cores [136]–[141] before the current wide usage of supermirrors in modern research reactors halls.

Correlated to this neutron total reflection phenomenon, the so-called frustrated total reflection observed with both thermal and cold neutrons is of major importance. Yet, it is of a fundamental curiosity; it was lacking with regard to deserved interest by the neutron scattering community until recent years when it was revived by Sears [142], Felcher *et al*. [143] and Ignatovich [144]. More precisely, this frustrated total reflection of neutron wave packets manifests itself by the existence of sharp dips in the plateau of total reflection due to the resonant bound states in nanostructured Fabry-Pérot like resonators [22]–[33], [36]–[37] as schematically shown in Figure 7(a).

The propagation of the neutron wave-packet within the various media of the Fabry-Pérot nanoresonator of Figure 7(a) is described by the time-independent Schrödinger equation (Equation 1) where h is the Planck constant, m the neutron mass, V_i and E_i are the Fermi potential and total energy in the medium "i" [130]. In this regime, the neutron wave

function ψ (r) is approximated by a plane wave $ei^{k.r}$ with the neutron wave vector k related to the De Broglie associated wavelength λ as $\lambda = (I2\pi/|k|)$ (Figure 7(b)). The conservation of the neutron's energy requires the momentum relation of equation (2) with k_0 and k_i denoting the magnitude of the neutron wave vector in vacuum and medium "i", respectively (Figure 2). In the continuum limit, the Fermi potential is $V_i = 2\pi h^2/m)(N_i \Sigma b_j)$ (Equation (3)) where b_j is the coherent scattering lengths of the nuclei in the medium "i" [130]. If one considers $\rho = N_i \Sigma b_j$ as the scattering length density of medium "i", the interaction/propagation of the neutron wave-packet in such a medium is described by the refractive index of equation (4).

$$[-h^2/2m\nabla^{2.} + V_i(r)]\ \psi(r) = E_i(r)]\ \psi(r) \quad (1)$$

$$h^2\ k_0^2/2m = h^2\ k_i^2/2m + V_i \quad (2)$$

$$V_i = (2\pi/m)h^2\ \rho_j,\ \rho_j = N_i\ \Sigma\ b_j \quad (3)$$

$$n_i = k_i/k_0 \sim 1\text{-}2\pi\ \rho_i/k_0^2 \quad (4)$$

$$\tanh(2\pi\ \sin\Theta\ d_R \tan(\phi)/\lambda) = \tan(2\phi)/\lambda)/\tan(2\pi\ \sin\Theta\ d_T/\lambda) \quad (5)$$

$$\tan(\phi) = ((\lambda/\lambda_C)^2 - 1)^{1/2},\ \lambda_C = \sin\Theta\ 1(\pi/\rho_R))^{1/2} \quad (6)$$

As in the case of X-ray photons [145], it is shown that in the case of a Fabry-Pérot nanostructure of Figure 1(a) consisting of two highly reflecting media ($\rho_j > 0$) separated by a neutron transparent medium ($\rho_j \leq 0$), the neutron wave-packets governed by the resonance condition equation (5) would suffer a frustrated total reflection corresponding to a neutron tunnelling through the first reflecting layer. This will be translated into the existence of specific dips in the plateau of total reflection. In view of the symmetry of the Fabry-Pérot nanoresonator, the tunnelled wave packets will resuffer the second tunnelling through the second reflecting layer. This second tunnelling will be observed henceforth in the transmitted beam. In summary, with a white (polyenergetic) neutron beam, all neutrons verifying the resonance condition of equations (5) and (6) will experience a first frustrated total reflection (tunnelling) and a second one through the reflecting media one and two, respectively. This is translated into the existence of several minima in the total reflection plateau and corresponding maxima in the transmitted beam, as validated in Figure 7(c).

Figure 7(c) displays the neutron reflectivity and transmission of a 200 Å Ni/2 000 Å V/200 Å Ni Fabry-Pérot nanoresonator deposited onto a 1 μm silicon substrate. The white neutron beam (λ = 2–20 Å) was impinging on the Fabry-Pérot nanoresonator under a grazing incidence Θ~0.8° with a relative angular resolution $\Delta\Theta/\Theta \cong 5\ 10^{-2}$, more precisely, the experimental neutron reflectivity R and transmission T in a linear scale versus neutron wavelength with the simulated curve (for reflectivity profile only). As one can notice, two main regions separated by the critical wavelength of nickel $\lambda C^{Ni} \sim 7.7$ Å are observed: the total reflection plateau and the so-called

vitreous region. In the vitreous region, a set of Kiessig fringes occur mainly due to the interference between the partial wave packets reflected at air-Ni, Ni-V and Ni-Si interfaces. Their simulation allows one to determine the films' thicknesses and their interfacial roughness. The obtained thicknesses are 200 A and 2 050 A for the Ni and V layers, respectively, while the interface roughness is constant, of the order of 7 Å.

The second region, which is the main feature of this contribution, is the total reflection plateau, where we clearly distinguish five resolved dips instead of the standard total reflection plateau (R = 100%). These dips, which clearly assert the frustrated total reflection in the considered Fabry-Pérot nanoresonator, correspond to the quasi-bound states (k = 1, 2, 3, 4 and 5). The characteristics of these resonances, which are correlated to the multiple internal reflections of the trapped neutron in the Fabry-Pérot nanoresonator, are summarised in Table 1. Each dip coincides with a tunnelled peak in the transmission curve. The width of these dips is different; the lower is the order, and the larger is the width at half maximum. As established, this is correlated to the neutron trapping time in the resonant cavity $\langle \tau_n \rangle_{Trapping}$. Via the Heisenberg uncertainty, the average associated value is of the order of $\langle \tau_n \rangle_{Trapping} \sim 2\pi m/(h\ k\ \Delta k)$. According to Table 1, this neutron trapping time in the resonant cavity $\langle \tau_n \rangle_{Trapping}$ varies approximately from 0.1 to 1 μs. It can be concluded that (i) neutrons with a De Broglie associated wavelength above 7 Å can be trapped within the considered 200 Å Ni/2 000 Å V/200 Å Ni Fabry-Pérot nanoresonator, (ii) such neutrons are trapped inside the transparent 2 000 V medium, totally reflected back and forth by the nickel layers at the internal Ni-V interfaces as schematically represented in the inset of Figure 3), and (iii) the higher the De Broglie wavelength, the higher the trapping time in the resonant cavity. Consequently, the European spallation source (ESS) might afford high flux cold or ultra-cold neutron beams, which are ideal for trapping in such Fabry-Pérot nanoresonators.

Table 1: Spectral parameters of the various minima in the total reflection plateau due to the frustrated total reflection in the 200 Å Ni/2 000 Å V/200 Å Ni /silicon substrate Fabry-Pérot nanoresonator, corresponding to the cavity quasi-bound states (υ = 1, 2, 3, 4 and 5). The derived trapping time $\tau \sim m/h\ k\ \Delta k$

Resonance order υ	**Resonance wavelength λ_{res}, (Å)**	**$\Delta\lambda_{res}$ (Å)**	**k, ($Å^{-1}$)**	**Δ k, (10^{-2} $Å^{-1}$)**	**Trapping time τ (ps)**
1	17.38	1.09	1.09	2.267	19.35
2	12.99	0.85	0.85	3.165	10.36
3	10.56	0.73	0.73	4.113	6.48
4	9.02	0.61	0.61	4.711	4.83
5	7.87	0.61	0.61	6.188	3.21

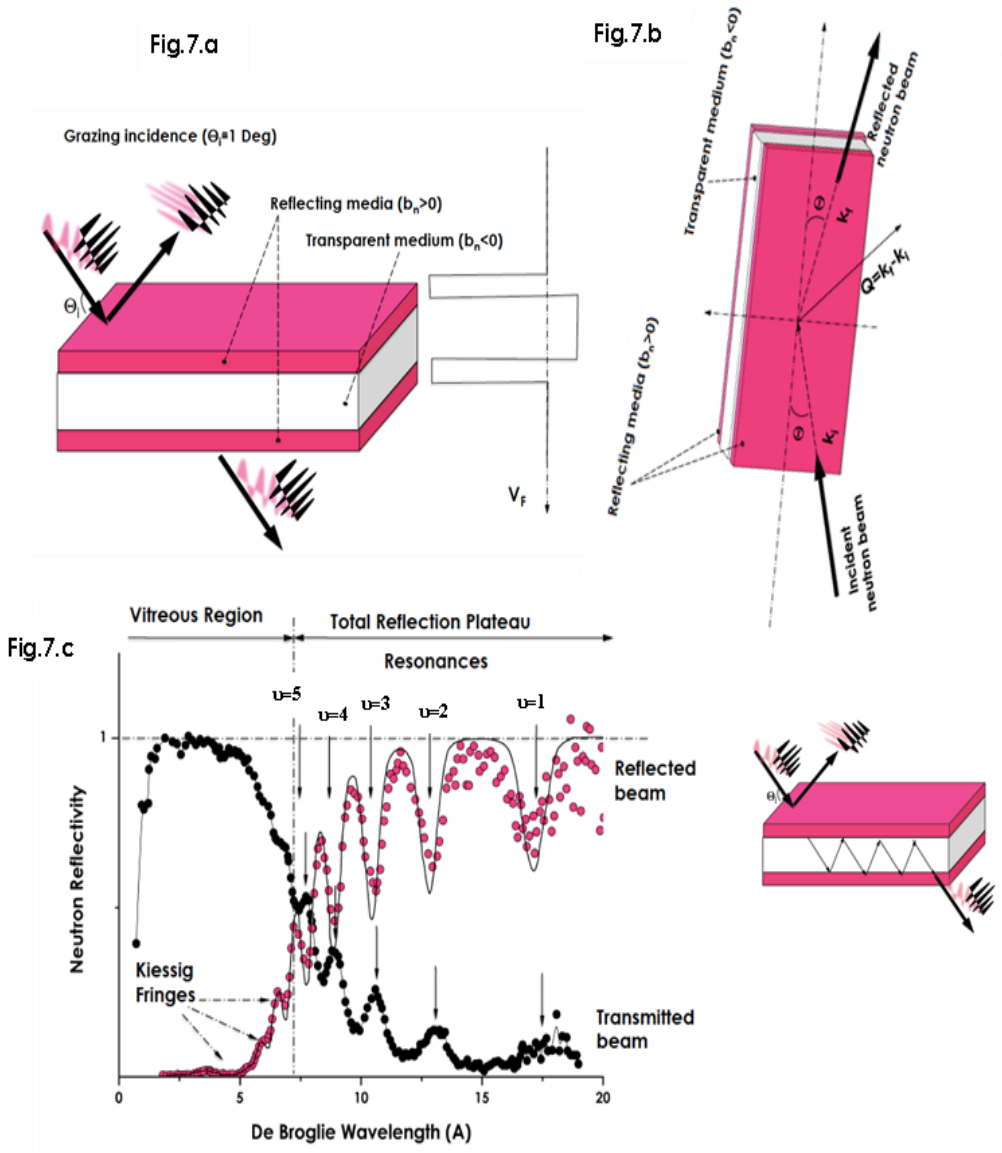

Figure 7: (a) Standard configuration of a thin film Fabry-Pérot resonator consisting of two identical high reflecting films separated by a transparent medium and the corresponding potential transversal distribution
(b): Standard neutron reflectometry configuration
(c): Neutron reflectivity and transmission of the 200 Å Ni/2000 Å V/200 Å Ni Fabry-Pérot nanoresonator deposited onto 1 μm silicon substrate. The white neutron beam (λ = 2–20 Å) was impinging on the Fabry-Pérot nanoresonator under a grazing incidence $\Theta \sim 0.8°$ with a relative angular resolution $\Delta\Theta/\Theta \cong 5\ 10^{-2}$

As a conclusion of this section, in which a nanoscaled Fabry-Pérot nanoresonator was used to trap cold neutrons with a De Broglie associated wavelength within the range of 2.5–25 Å, the following can be deduced:

- cold neutrons manifested their wave-particle duality via a Ni/V/Ni/Si substrate resonating nanostructure;
- double tunnelling occurred through the high-reflecting Ni nanobarriers;
- the resonating neutron were efficiently trapped within the V spacing film;
- neutrons with a higher De Broglie wavelength have been trapped for a longer time within the nanoscaled resonator; and
- as it is derived from the Heisenberg uncertainty, this neutron trapping time is of the highest precision so far and could contribute to the neutron lifetime investigations of special importance to cosmology.

8 Conclusions

In this minireview, we considered a series of examples to shed light on the size effects at the nanoscale. Within such nanosystems, the following was determined:

- the intrinsic luminescence of ZnO nanodiscs was found depending on their basal thickness D. More precisely:
  - the maximum of the excitonic emission λ^{max} shifts to lower values when the ZnO nanodiscs thickness $< D >$ decreases ($\lambda^{max} \sim < D >$),
  - the excitonic peak's width at half maximum $\Delta \lambda_{1/2}$ is basal size-dependent; it becomes sharp when the ZnO nanodiscs' thickness$< D>$ decreases ($\Delta \lambda_{1/2} \sim 1/< D >$);
- the thermodynamic of melting and sublimation of NaCl nanocrystals were size-dependent versus their transversal thickness $< D_{Trans} >$:
  - the sublimation temperature is size-dependent as $T_{sub}\ \alpha\ (D_{Trans})^2$,
  - the smallest nanocrystals of NaCl with D_{Trans}= 63.5 nm start sublimating below 323.5 K, far below the bulk value of 1 686 K;
- the quantum confinement of phonons in nanoscaled particles of anatase TiO_2. This was observed through the width at half maximum and the Raman spectral position of the major Eg vibrational mode of TiO_2 nanoparticles;
- the liquid–solid phase transition in nanoscaled systems is size driven via surface tension considerations. More precisely, it was found that for Hg nanoparticles with diameter $Ø_{nano\text{-}Hg} < 2.50$ nm, the excess surface pressure is ΔP above 0.76 GPa at RT, inducing a net crystallisation at RT. This translates into a net atomic ordering of about seven to eight atomic reticular plans of the hexagonal;

- a strong Anderson localisation at RT of IR radiations in ship-shaped CNTs validating the possibility of a particularly unexpected resonance of electromagnetic waves in disordered media; and
- neutrons can be trapped in Fabry-Pérot nanoscaled resonators, highlighting their wave-particle duality. Governed by the Heisenberg uncertainty, such a trapping time approach could be used or linked to the neutron lifetime of pivotal importance in cosmology and nuclear physics.

9 References

[1] C. N. R. Rao, and K. Biswas, "Characterization of nanomaterials by physical methods," *Annu. Rev. Anal. Chem*, vol. 2, no. 1, pp. 435–462, 2009, doi: 10.1146/annurev-anchem-060908-155236.

[2] A. Santamaria, "Historical overview of nanotechnology and nanotoxicology," in *Methods in Molecular Biology: Nanotoxicity*, J. Reineke, Ed., Totowa, NJ, United States: Humana, 2012, pp: 1–12, doi: 10.1007/978-1-62703-002-1_1.

[3] N. Taniguchi, "On the basic concept of nanotechnology," in *Proc. of the Int. Conf. on Prod. Eng.*, 1974, pp. 18–23.

[4] R. Feynman, "There's plenty of room at the bottom," *Eng. Sci.*, vol. 23, pp. 22–36, 1960.

[5] N. Baig, I. Kammakakam, and W. Falath, "Nanomaterials: A review of synthesis methods, properties, recent progress, and challenges," *Mater. Adv*., vol. 2, pp. 1821–1871, 2021, doi: 10.1039/D0MA00807A.

[6] M. J. Mitchell, M. M. Billingsley, R. M. Haley, M. E. Wechsler, N. A. Peppas, and R. Langer, "Engineering precision nanoparticles for drug delivery," *Nat. Rev. Drug. Discov*., vol. 20, no. 2, pp. 101–124, 2021, doi: 10.1038/s41573-020-0090-8.

[7] M. Jeyaraj, S. Gurunathan, M. Qasim, M. H. Kang, and J. H. Kim, "A comprehensive review on the synthesis, characterization, and biomedical application of platinum nanoparticles," *J. Nanomater*., vol. 9, p. 1719, 2019, doi: 10.3390/nano9121719.

[8] C. M. Lieber, and C. C. Chen, "Solid state physics—Advances in research and applications, *AP*, vol. 48, pp. 109–148, 1994, doi: 10.1016/S0081-1947(08)60578-0.

[9] J. Jeevanandam, A. Barhoum, Y. S. Chan, A. Dufresne, and M. K. Danquah, "Review on nanoparticles and nanostructured materials: History, sources, toxicity and regulations," *Beilstein J. Nanotechnol*., vol. 9, pp. 1050–1074, 2018, doi: 10.3762/bjnano.9.98.

[10] H. Ago, *Frontiers of Graphene and Carbon Nanotubes*, Tokyo, Japan: Springer, 2015, doi: 10.1007/978-4-431-55372-4_1.

[11] Y. C. Kong, D. P. Yu, B. Zhang, B., W. Fang, and Q. Feng, "Ultraviolet-emitting ZnO, nanowires synthesized by a physical vapor deposition approach," *Appl. Phys. Lett*., vol. 78, no. 4, p. 407, 2001, doi: 10.1063/1.1342050.

[12] H. Cao, Y. G. Zhao, S. T. Ho, E. W. Seelig, Q. H. Wang, and R. P. H. Chang, "Random laser action in semiconductor powder," *Phys. Rev. Lett*., vol. 82, no. 11, p. 2278, 1999, doi: 10.1103/PhysRevLett.82.2278.

[13] L. Guo, *et al*., "Synthesis and characterization of poly(vinylpyrrolidone)-modified zinc oxide nanoparticles," *Chem. Mater*., vol. 12, P. 2268, 2000, doi: 10.1021/cm9907817.

[14] B. D. Ngom, T. Mpahane, E. Manikandan, and M. Maaza, "ZnO nano-discs by lyophilization process: Size effects on their intrinsic luminescence," *J. Alloys Compd*., vol. 656, pp. 758–763, 2016, doi: 10.1016/j.jallcom.2015.09.230.

[15] X. Y. Kong, and Z. L. Wang, "Spontaneous polarization-induced nanohelixes, nanosprings, and nanorings of piezoelectric nanobelts," *Nano Lett*., vol. 3, no. 12, p. 1625, 2003, doi: 10.1021/nl034463p.

[16] M. Joseph, H. Tabata, and T. Kawai, "P-type electrical conduction in ZnO thin films by Ga and N cooping," *Jpn J. Appl. Phys. Part 2 Lett*., vol. 38, p. L1205, 1999, doi: 10.1143/JJAP.38.L1205.

[17] J. Kennedy, D. A. Carder, and A. Markwitz, R. J. Reeves, "Properties of nitrogen implanted and electron beam annealed bulk ZnO," *J. Appl. Phys*., vol. 107, p. 103518, 2010, doi: 10.1063/1.3380592.

[18] J. Kennedy, P. P. Murmu, and E. Manikandan, S. Y. Lee, "Investigation of structural and photoluminescence properties of gas and metal ions doped zinc oxide single crystals," *J. Alloys Compd*., vol. 616, p. 614e617, 2014, doi: 10.1016/j.jallcom.2014.07.179.

[19] F. Fang, J. Futter, A. Markwitz, and J. Kennedy, "UV and humidity sensing properties of ZnO nanorods prepared by the arc discharge method," *J. Nanotechnol*., vol. 20, p. 245502, 2009, doi: 10.1088/0957-4484/20/24/245502.

[20] J. C. Thomas, and A. van der Ven, "Finite-temperature properties of strongly anharmonic and mechanically unstable crystal phases from first principles," *Phys. Rev. B*, vol. 88, p. 214111, 2013, doi: 10.1103/PhysRevB.88.214111.

[21] M. Haase, H. Weller, and A. Henglein, "Photochemistry and radiation chemistry of colloidal semiconductors. 23. Electron storage on ZnO particles & size quantization, *J. Phys. Chem*., vol. 92, p. 482, 1988, doi: 10.1021/j100313a047.

[22] F. Buda, J. Kadanoff, and M. Parinello, "Optical properties of porous silicon: A first principles study," *Phys. Rev. Lett*., vol. 69, p. 1272, 1992, doi: 10.1103/PhysRevLett.69.1272.

[23] G. Hearne, *et al*., "Effect of grain size on structural transitions in anatase TiO2: A Raman spectroscopy study at high pressure," *Phys. Rev. B*, vol. 70, no. 13, p. 134102, 2004, doi: 10.1103/PhysRevB.70.134102.

[24] V. L. Colvin, M. C. Schlamp, and A. P. Alivisatos, "Light-emitting diodes made from cadmium selenide nanocrystals and a semiconducting polymer," *Nature*, vol. 370, p. 354, 1994, doi: 10.1038/370354a0.

[25] L. E. Brus, "Electronic wave functions in semiconductor clusters: Experiment and theory," *J. Phys. Chem.*, vol. 90, p. 2555, 1986, doi: 10.1021/j100403a003.

[26] R. Viswanatha, S. Sapra, B. Satpati, P. V. Satyam, B. N. Dev, and D. D. Sama, "Understanding the quantum size effects in ZnO nanocrystals," *J. Mater. Chem*., vol. 14, p. 661, 2004, doi: 10.1039/b310404d5.

[27] O. Madelung, Ed. Data in Science and Technology, Semiconductors Other than Group IV Elements and III-V Compounds, Berlin, Germany: Springer, 1992.

[28] E. A. Meulenkamp, "Synthesis and growth of ZnO nanoparticles," *J. Phys. Chem. B*, vol. 102, p. 5566, 1998, doi: 10.1021/jp980730h.

[29] E. M. Wong, J. E. Bonevich, and P. C. Pearson, "Ultrafast studies of photoexcited electron dynamics in g- and a-Fe2O3 semiconductor nanoparticles," *J. Phys. Chem. B*, vol. 102, no. 770, 1998, doi: 10.1021/jp982397n.

[30] S. Cho, *et al*., "Photoluminescence and ultraviolet lasing of polycrystalline ZnO thin films by the oxidation of the metallic Zn," *Appl. Phys. Lett*., vol. 75, p. 2761, 1999, doi: 10.1063/1.125141.

[31] A. Studenikin, N. Golego, and M. Cocivera, "Fabrication of green and orange photoluminescent, undoped ZnO films using spray pyrolysis," *J. Appl. Phys*., vol. 84, p. 2287, 1998, doi: 10.1063/1.368295.

[32] H. J. Ko, T. Yao, Y. Chen, and S. K. Hong, "Investigation of ZnO epilayers grown under various Zn/O ratios by plasma-assisted molecular-beam epitaxy," *J. Appl. Phys*., vol. 92, p. 4354, 2002, doi: 10.1063/1.1509103.

[33] T. Koida, S. F. Chichibu, and A. Uedono, "Correlation between the photoluminescence lifetime and defect density in bulk and epitaxial ZnO," *Appl. Phys. Lett*., vol. 82, p. 532, 2003, doi: 10.1063/1.1540220.

[34] S. Bethke, H. Pan, and B.W. Wessels, "Luminescence of heteroepitaxial zinc oxide," *Appl. Phys. Lett*., vol. 52, p. 138, 1988, doi: 10.1063/1.99030.

[35] Y. Hen, *et al*., "Plasma assisted molecular beam epitaxy of ZnO on c -plane sapphire: growth and characterization," *J. Appl. Phys*., vol. 84, p. 3912, 1998, doi: 10.1063/1.368595.

[36] Z. W. Pan, Z. R. Dai, and Z. L. Wang, "Nanobelts of semiconducting oxides," *Science*, vol. 291, p. 1947, 2001, doi: 10.1126/science.1058120.

[37] B. D. Ngom, M. Chaker, N. Manyala, B. Lo, M. Maaza, and A. C. Beye, "Temperature-dependent growth mode of W-doped ZnO nanostructures," *Appl. Surf. Sci.*, vol. 257, p. 6226e6232, 2011, doi: 10.1016/j.apsusc.2011.02.043.

[38] B. D. Ngom, *et al*., "Structural, morphological and photoluminescence properties of W-doped ZnO nanostructures," *Appl. Surf. Sci*., vol. 255, p. 7314e7318, 2009, doi: 10.1016/j.apsusc.2009.03.089.

[39] M. Kaidashev, *et al*., "High electron mobility of epitaxial ZnO thin films on c-plane sapphire grown by multistep pulsed-laser deposition," *Appl. Phys. Lett*., vol. 82, no. 32, p. 3901, 2003, doi: 10.1063/1.1578694.

[40] X. D. Wang, Y. Ding, C. J. Summers, and Z. L. Wang, "Large-scale synthesis of six-nanometer-wide ZnO nanobelts," *J. Phys. Chem. B*, vol. 108, p. 8773e8777, 2004, doi: 10.1021/jp048482e.

[41] Z. Qiu, K. S. Wong, M. Wu, W. Lin, and H. Xu, "Microcavity lasing behavior of oriented hexagonal ZnO nanowhiskers grown by hydrothermal oxidation," *Appl. Phys. Lett*., vol. 84, no. 15, p. 2739, 2004, doi: 10.1063/1.1697633.

[42] S. H. Tolbert, and A. P. Alivisatos, "The Wurtzite to rock salt structural transformation in CdSe nanocrystals under high pressure," *J. Chem. Phys*., vol. 102, p. 4642, 1995, doi: 10.1063/1.469512.

[43] I. Shalish, H. Temkin, and V. Narayamurti, "Size-dependent surface luminescence in ZnO nanowires," *Phys. Rev. B*, vol. 69, p. 245401, 2004, doi: 10.1103/PhysRevB.69.245401.

[44] O. I. Micic, J. R. Sprague, Z. Lu, and A. J. Nozik, "Highly efficient band-edge emission from InP quantum dots," *Appl. Phys. Lett*., vol. 68, p. 3150, 1996, doi: 10.1063/1.115807.

[45] O.I. Micic, *et al*., "Size-dependent spectroscopy of InP quantum dots," *J. Phys. Chem. B*, vol. 101, p. 4904, 1997, doi: 10.1021/jp9704731.

[46] Ph. Buffat, and J-P. Borel, "Size effect on the melting temperature of gold particles," *Phys. Rev. A*, vol. 13, p. 2287, 1976, doi: 10.1103/PhysRevA.13.2287.

[47] N. Kana, S. Khamlich, J. B. Kana Kana, and M. Maaza, "Peculiar surface size-effects in NaCl nanocrystals," *Surf. Rev. Lett*., vol. 20, no. 1, p. 1350001, 2013, doi: 10.1142/S0218625X13500017.

[48] W. P. Halperin, "Quantum size effects in metal particles," *Rev. Mod. Phys*., vol. 58, p. 533, 1986, doi: 10.1103/RevModPhys.58.533.

[49] V. P. Skripov, V. P. Koverda, and V. N. Skokov, “Size effect on melting of small particles,” *Phys. Status Solidi*, vol. 66, pp. 109–118, 1981, doi: 10.1002/pssa.2210660111.

[50] A. Heidenreich, I. Oref, and J. Jortner, “Isomerization dynamics of sodium chloride tetrameric clusters,” *J. Chem. Phys*., vol. 96, no. 19, pp. 7517–7523, 1992, doi: 10.1021/j100198a010.

[51] U. Landman, D. Scharf, and J. Jortner, “Electron localization in alkali-halide clusters,” *Phys. Rev. Lett*., vol. 54, no. 16, p. 1860, 1985, doi: 10.1103/PhysRevLett.54.1860.

[52] D. Scharf, J. Jortner, and U. Landman, “Cluster isomerization induced by electron attachment,” *J. Chem. Phys*., vol. 87, pp. 2716–2723, 1987, doi: 10.1063/1.453059.

[53] D. Patterson, J. A. Morrison, and F. W. Thompson, “Low temperature particle size effect on the heat capacity of NaCl,” *Can. J. Chem*., vol. 33, no. 2, pp. 240–244, 1955, doi: 10.1139/v55-027.

[54] J. E. Campana, T.M. Barlak, R. Colton, J. J. DeCorpo, J. R. Wyatt, and B. I. Dunlap., “Effect of cluster surface energies on secondary-ion-intensity distributions from ionic crystals,” *Phys. Rev. Lett*., vol. 47, pp. 1046–1049, 1981, doi: 10.1103/PhysRevLett.47.1046.

[55] T. P. Martin, “Alkali halide clusters and microcrystals,” *Phys. Rep*., vol. 95, no. 3, pp. 167–199, 1983, doi: 10.1016/0370-1573(83)90024-8.

[56] R. L. Whetten, “Alkali halide nanocrystals,” *Acc. Chem. Res*., vol. 26, no. 2, pp. 49–56, 1993, doi: 10.1021/ar00026a003.

[57] J. E. Lester, and G. A. Somorjai, “The effect of dislocations on the vaporization rate of NaCl single crystals,” *Appl. Phys. Lett*., vol. 12, p. 216, 1968, doi: 10.1063/1.1651959.

[58] R. R. Hudgins, Ph. Dugourd, J. M. Tanenbaum, and M. F. Jarold, “Structural transitions in sodium chloride nanocrystals,” *Phys. Rev. Lett*., vol. 78, p. 421, 1997, doi: 10.1103/PhysRevLett.78.4213.

[59] *GmeLin Handbook of Inorganic Chemistry*, 8th ed. Berlin, Germany: Springer, 1928.

[60] P.R. Couchman, and W. A. Jesser, “Thermodynamic theory of size dependence of melting temperature in metals,” *Nature*, vol. 269, pp. 481–483, 1977, doi: 10.1038/269481a0.

[61] D. Bersani, P. P. Lottici, and X-Z. Ding, “Phonon confinement effects in the Raman scattering by TiO_2 nanocrystals,” *Appl. Phys. Lett*., vol. 72, no. 1, pp. 73–75, 1998, doi: 10.1063/1.120648.

[62] H. Richter, Z. P. Wang, and L. Ley, "The one phonon Raman spectrum in microcrystalline silicon," *Solid State Commun*., vol. 39, no. 5, pp. 625–629, 1981, doi: 10.1016/0038-1098(81)90337-9.

[63] I. H. Campbell, and P. M. Fauchet, "The effects of microcrystal size and shape on the one phonon Raman spectra of crystalline semiconductors," *Solid State Commun*., vol. 58, no. 10, pp. 739–741,1986, doi: 10.1016/0038-1098(86)90513-2.

[64] D. R. dos Santos, and I. L. Torriani, "Crystallite size determination in μc-Ge films by x-ray diffraction and Raman line profile analysis," *Solid State Commun*., vol. 85, no. 4, pp. 307–310, 1993, doi: 10.1016/0038-1098(93)90021-E.

[65] D. Bersani, and P. P. Lottici, "Confinement effects on the LO-phonons in $CdSe_xS_{1-x}$ doped glasses," *Phys. Status Solidi B*, vol. 174, no. 2, pp. 575–582, 1992, doi: 10.1002/pssb.2221740227.

[66] A. Tu, and P. D. Persans, "Raman scattering as a probe of composition in II–VI ternary semiconductor-glass composites," *Appl. Phys. Lett*., vol. 58, p. 1506, 1991, doi: 10.1063/1.105160.

[67] C. E. Bottani, *et al*., "Raman, optical-absorption, and transmission electron microscopy study of size effects in germanium quantum dots." *Appl. Phys. Lett*., vol. 69, no. 16, pp. 2409–2411, 1996, doi: 10.1063/1.117653.

[68] P. P. Lottici, D. Bersani, M. Braghini, and A. Montenero, "Raman scattering characterization of gel-derived titania glass," *J. Mater. Sci*., vol. 28, pp. 177–183, 1993, doi: 10.1007/BF00349049.

[69] T. Ohsaka, S. Yamahoka, and O. Shimomura, "Effect of hydrostatic pressure on the Raman spectrum of anatase (TiO_2)," *Solid State Commun*., vol. 30, no. 6, pp. 345–347, 1979, doi: 10.1016/0038-1098(79)90648-3.

[70] J. Traylor, H. G. Smith, R. M. Nicklow, and M. K. Wilkinson, "Lattice dynamics of rutile," *Phys. Rev. B*, vol. 3, p. 3457, 1971, doi: 10.1103/PhysRevB.3.3457.

[71] P. Pyykkö, "Relativistic effects in structural chemistry," *Adv. Quantum Chem*., vol. 11, p. 353, 1978, doi: 10.1016/S0065-3276(08)60241-5.

[72] M. C. Wilkinson, "Surface properties of mercury," *Chem. Rev*., vol. 72, no. 6, pp. 575–625, 1972, doi: 10.1021/cr60280a001.

[73] R. Evans, "The Monte Carlo method for the study of phase transitions: A review of some recent progress," *J. Phys. C*, vol. 7, p. 2808, 1974.

[74] S. Amokrane, *et al*., "A pseudo-atom theory for the liquid-vapor interface of simple metals," *J. Phys. Chem*., vol. 75, p. 5543, 1982, doi: 10.1063/1.441959.

[75] N. D. Lang, *et al*., "Theory of metal surfaces," *Phys. Rev. B*, vol. 12, p. 4555, 1970, doi: 10.1103/PhysRevB.1.4555.

[76] E. Chacon, *et al*., "Nonlocal kinetic energy functional for nonhomogeneous electron systems," *Phys. Rev. B*, vol. 32, p. 7868, 1985, doi: 10.1103/PhysRevB.32.7868.

[77] M. A. Gomez, *et al*., "Electronic structure: wide-band, narrow-band, and strongly correlated systems," *Phys. Rev. B*, vol. 46, p. 6665, 1992.

[78] M. Magnussen, *et al*., "X-ray reflectivity measurements of surface layering in liquid mercury," *Phys. Rev. Lett*., vol. 74, no. 22, p. 4444, 1995, doi: 10.1103/PhysRevLett.74.4444.

[79] U. Bafile, *et al*., "Neutron diffraction on mercury: Density dependence of the static structure factor," *J. Non-Cryst. Solids.*, vol. 35, pp. 250–252, 1999, doi: 10.1016/S0022-3093(99)00210-0.

[80] U. Bafile, *et al*., "The microscopic structure of liquid mercury from neutron and X-ray diffraction," *Physica. B*, vol. 452, pp. 276–278, 2000, doi: 10.1016/S0921-4526(99)01671-3.

[81] D. A. Young, *Phase Diagram of Elements*. Los Angeles, CA: University of California, 1991, doi: 10.1525/9780520911482.

[82] T. Matsui, *et al*., "Synthesis and characterization of cerium oxide nanoparticles coated with turbostratic boron nitride," *J. Mater. Chem*., vol. 13, pp. 622–627, 2003, doi: 10.1039/b208109a.

[83] N. Gaston, *et al*., "The lattice structure of mercury: Influence of electronic correlation," *Phys. Rev. B*, vol. 74, p. 094102, 2006, doi: 10.1103/PhysRevB.74.094102.

[84] F. R. S. Rayleigh, "On the electromagnetic theory of light," *Lond. Edinb. Dublin Philos. Mag. J. Sci*., vol. 12, no. 73, pp. 81–101, 1881, doi: 10.1080/14786448108627074.

[85] F. R. S. Rayleigh, "XXXIV. On the transmission of light through an atmosphere containing small particles in suspension, and on the origin of the blue of the sky," *Lond. Edinb. Dublin Philos. Mag. J. Sci*., vol. 47, no. 287, pp. 375–384, 1981, doi: 10.1080/14786449908621276.

[86] G. Mie, "Beiträge zur Optik trüber Medien, speziell kolloidaler Metallösungen," *Ann. Phys*., vol. 330, no. 3, pp. 377–445, 1908, doi: 10.1002/andp.19083300302.

[87] W. Hergert, and T. Wriedt, *The Mie Theory*. Berlin, Germany: Springer, 2012. doi: 10.1007/978-3-642-28738-1.

[88] M. Wang, M. Cao, Z. R. Guo, and N. Gu, "Generalized multiparticle Mie modeling of light scattering by cells," *Chin. Sci. Bull*., vol. 58, no. 21, pp. 2663–2666, 2013, doi: 10.1007/s11434-013-5719-0.

[89] P. W. Anderson, “Absence of diffusion in certain random lattices,” *Phys. Rev*., vol. 109, pp. 1492–1505, 1958.

[90] D. J. Thouless, “Anderson’s theory of localized states,” *J. Phys. C: Solid State Phys*., vol. 4, p. 1559, 1970, doi: 10.1103/PhysRev.109.1492.

[91] P. W. Anderson, “Local moments and localized states,” *Rev. Mod. Phys*., vol. 50, p. 191, 1978, doi: 10.1103/RevModPhys.50.191.

[92] D. C. Licciardello, and D. J. Thouless, “Constancy of minimum metallic conductivity in two dimensions,” *Phys. Rev. Lett*., vol. 35, p. 1475, 1974, doi: 10.1103/PhysRevLett.35.1475.

[93] H.G. Schuster, “On a relation between the mobility edge problem and an isotropic XY model,” *Zeitschrift für Physik B Condensed Matter*, vol. 31, pp. 99–104, 1978, doi: 10.1007/BF01320130.

[94] W. Anderson, D. C. Licciardello, and T. V. Ramakrishnan, “Scaling theory of localization: Absence of quantum diffusion,” *Phys. Rev. Lett*., vol. 42, p. 673, 1979, doi: 10.1103/PhysRevLett.42.673.

[95] N. F. Mott, and W. D. Twose, “The theory of impurity conduction,” *Adv. Phys*., vol. 10, p. 107, 1961, doi: 10.1080/00018736100101271.

[96] D. S. Wiersma, M. P. Albada, B. A. van Tiggelen, and A. Lagendijk, “Experimental evidence for recurrent multiple scattering events of light in disordered media,” *Phys. Rev. Lett*., vol. 74, pp. 4193–4196, 1995, doi: 10.1103/PhysRevLett.74.4193.

[97] D. S. Wiersma, P. Bartolini, A. Lagendijk, and R. Righini, “Localization of light in a disordered medium,” *Nature*, vol. 390, pp. 18–25, 1997, doi: 10.1038/37757.

[98] H. Cao, A. Yamilov, J.Y. Xu, E. Seelig, and R. Chang, “Lasing in disordered media,” *Proc. SPIE—The Int. Soc. Opt. Eng*., vol. 4995, pp. 134–143, 2003, doi: 10.1117/12.479757.

[99] A. Maslov, and C. Z. Ning, “Reflection of guided modes in a semiconductor nanowire laser,” *Appl. Phys. Lett*., vol. 83, p. 1237, 2003, doi: 10.1063/1.1599037.

[100] R. Dalichaouch, J. P. Armstrong, S. Schultz, P. M. Platzman, and S. L. McCall, “Microwave localization by two-dimensional random scattering,” *Nature*, vol. 354, pp. 53–55, 1991, doi: 10.1038/354053a0.

[101] E. Abrahams, P. W. Anderson, D. C. Licciardello, and T. V. Ramakrishnan, “Scaling theory of localization: Absence of quantum diffusion in two dimensions,” *Phys. Rev. Lett*., vol. 42, pp. 673–676, 1979, doi: 10.1103/PhysRevLett.42.673.

[102] R. Kaiser, T. Jonckheere, A. Müller, C. Miniatura, and D. Delande, “Multiple scattering of light by atoms in the weak localization regime,” *Phys. Rev. Lett*., vol. 85, no. 20, pp. 4269–4272, 2000, doi: 10.1103/PhysRevLett.85.4269.

[103] J. X. Zhu, D. J. Pine, and D. A. Weitz, “Internal reflection of diffusive light in random media,” *Phys. Rev. A*, vol. 44, pp. 3948–3957, 1991, doi: 10.1103/PhysRevA.44.3948.

[104] K. Arya, Z. B. Su, and J. L. Birman, “Anderson localization of electromagnetic waves in a dielectric medium of randomly distributed metal particles,” *Phys. Rev. Lett*., vol. 57, pp. 2725–2728, 1986, doi: 10.1103/PhysRevLett.57.2725.

[105] J. Bertolotti, S. Gottardo, D. S. Wiersma, M. Ghulinyan, and L. Pavesi, “Optical necklace states in Anderson localized 1D systems,” *Phys. Rev. Lett*., vol. 94, p. 113903, 2005, doi: 10.1103/PhysRevLett.94.113903.

[106] S. Karbasi, C. R. Mirr, R. J. Frazier, P. G. Yarandi, K. W. Koch, and A. Mafi, “Transverse Anderson localization in a disordered glass optical fiber,” *Opt. Express*, vol. 20, no. 17, pp. 18692–18706, 2012, doi: 10.1364/OE.20.018692.

[107] S. Karbasi, T. Hawkins, J. Ballato, K. W. Koch, and A. Mafi, “Advances in the fabrication of disordered transverse Anderson localizing optical fibers,” *Opt. Mater. Express*, vol. 2, no. 11, pp. 1496–1503, 2012, doi: 10.1364/OME.2.001496.

[108] M. Maaza, *et al*., “On the possible optical resonance in carbon nanotubes based cavities,” *Int. J. Nanotechnol*., vol. 4, pp. 638–650, 2007, doi: 10.1504/IJNT.2007.015460.

[109] M. Maaza, and C. N. R. Rao, “Anderson localization of IR light in 1D nanosystems,” *J. Opt. Soc. Am. A*, vol. 37, no. 11, pp. C111–C117, 2020, doi: 10.1364/JOSAA.394917.

[110] C. N. R. Rao, and A. Govindaraj, “Organometallic precursor route to carbon nanotubes,” *Pure Appl. Chem*., vol. 74, no. 9, p. 1571, 2002, doi: 10.1351/pac200274091571.

[111] O. Lummer, and E. Gehrcke, “On the diffraction of light incident at nearly the critical angle on the boundary between two media,” *Ann. Phys. Band*, vol. 10, p. 457, 1903, doi: 10.1002/andp.19033150302.

[112] M. Born, and E. Wolf, *The Lummer-Gehrcke Interferometer*. *Principles of Optics*, 7th ed. Cambridge, UK: CUP, 1999.

[113] J. K. Robertson, “Computation of correlated color temperature and distribution temperature,” *J. Opt. Soc. Am*., vol. 11, no. 5, pp. 559–563, 1925.

[114] D. S. Wiersma, P. Bartolini, A. Lagendijk, and R. Righini, “Localization of light in a disordered medium,” *Nature*, vol. 390, p. 671, 1997, doi: 10.1038/37757.

[115] A. A. Chabanov, and A. Z. Genack, “Statistics of dynamics of localized waves,” *Phys. Rev. Lett*., vol. 87, p. 233903, 2001, doi: 10.1103/PhysRevLett.87.233903.

[116] P. Sheng, *Introduction to Wave Scattering, Localization, and Mesoscopic Phenomena*. New York, NY: AP, 1995, doi: 10.1016/B978-012639845-8/50010-1.

[117] J. A. Sanchez-Gil, and V. Freilikher, "Resonances in the one-dimensional Anderson localization," *Phys. Rev. B*, vol. 68, p. 075103, 2003, doi: 10.1103/PhysRevB.68.075103.

[118] K. Y. Bliokh, Y. P. Bliokh, and V. Freilikher, "Resonances in one-dimensional disordered systems," *J. Opt. Soc. Am. B*, vol. 21, p. 113, 2004, doi: 10.1364/JOSAB.21.000113.

[119] S. X. Zhu, D. J. Pine, and D. A. Weitz., "Internal reflection of diffusive light in random media," *Phys. Rev. A*, vol. 44, no. 6, p. 3948, 1991, doi: 10.1103/PhysRevA.44.3948.

[120] A. Steyerl, K. A. Steinhauser, H. Sheckenhofer, and S. S. Malik, "Observation of quasibound states of the neutron in matter," *Phys. Rev. Lett.*, vol. 44, p. 1306, 1980, doi: 10.1103/PhysRevLett.44.1306.

[121] A. Steyerl, T. Ebisawa, K. A. Steinhauser, and M. Utsuro, "Experimental study of macroscopic coupled resonators for neutron waves," *Zeitschrift für Physik B Cond. Matt.*, vol. 41, pp. 283–290, 1981, doi: 10.1007/BF01307316.

[122] A. Steyerl, W. Drexel, S. S. Malik, and E. Gutsmeidl, "Neutron resonators and interferometers for very low energy neutrons," *Physica B+C*, vol. 151, no. 1–2, pp. 36–43, 1988, doi: 10.1016/0378-4363(88)90142-8.

[123] M. Maaza, and D. Hamidi, "Nano-structured Fabry-Pérot resonators in neutron optics & tunneling of neutron wave-particles," *Phys. Rep.*, vol. 514, no. 5, pp. 177–198, 2012, doi: 10.1016/j.physrep.2012.01.005.

[124] M. Maaza, B. Pardo, J. P. Chauvineau, A. Raynal, A. Menelle, and F. Bridou, "Neutron tunneling and neutron lifetime in a Ni-V-Ni Fabry-Perot thin film resonator," *Phys. Lett.*, vol. 223, no. 3, pp. 145–148, 1996.

[125] M. Maaza, *et al.*, "Zeeman neutron tunneling in Ni-Co-Ni thin film resonators," *Phys. Lett. A*, vol. 235, no. 1, pp. 19–23, 1997, doi: 10.1016/S0375-9601(97)00571-9.

[126] M. Maaza, *et al.*, "Shearing neutron interferometry and possibilities of studying interfacial diffusion processes between two highly dilute solutions," *Phys. Lett. A*, vol. 195, no. 1, pp. 1–8, 1994.

[127] A. Matiwane, J. Sackey, M. L. Lekala, A. Gibaud, and M. Maaza, "Neutron tunneling in nanostructured systems: Isotopical effect," *MRS Adv.*, vol. 3, no. 42–43, pp. 2609–2616, 2018, doi: 10.1557/adv.2018.228.

[128] M. Maaza, L. P. Chernenko, D. A. Korneev, B. Pardo, C. Sella, and F. Bridou, “A way to reach high accuracy in the determination of the magnetic London penetration depth in superconductors by polarized neutron reflectometry,” *Phys. Lett. A*, vol. 218, no. 3–6, pp. 312–318, 1996, doi: 10.1016/0375-9601(96)00415-X.

[129] M. Maaza, *et al*., “Monochromation and apodization with Ti-B4C multilayers in neutron optics,” *Phys. B: Phys. Condens. Matter*, vol. 198, no. 1–3, pp. 231–234, 1994, doi: 10.1016/0921-4526(94)90167-8.

[130] V. F. Sears, Neutron optics: An introduction to the theory of neutron optical phenomena and their applications. Oxford: UK: OUP, 1989.

[131] C. G. Shull, “Single-slit diffraction of neutrons,” *Phys. Rev*., vol. 179, p. 752, 1969, doi: 10.1103/PhysRev.179.752.

[132] H. Maier-Leibnitz, and T. Springer, “Ein Interferometer für langsame Neutronen,” *Zeitschrift für Physik*, vol. 167, pp. 386–402, 1962, doi: 10.1007/BF01378119.

[133] F. J. Landkammer, “Beugungsversuche mit langsamen Neutronen,” *Zeitschrift für Physik*, vol. 189, pp. 113–137, 1966, doi: 10.1007/BF01327150.

[134] H. Kurz, and H. Rauch, “Diffraction of thermal neutrons by a ruled grating,” *Zeitschrift für Physik*, vol. 220, pp. 419–426, 1969, doi: 10.1007/BF01394786.

[135] H. Rauch, W. Treimer, and U. Bonse, “Test of a single crystal neutron interferometer,” *Phys. Lett. A*, vol. 47, no. 5, pp. 369–371, 1974, doi: 10.1016/0375-9601(74)90132-7.

[136] B. P. Schoenborn, D.L. D. Caspar, and O. F. Kammerer, “A novel neutron monochromator,” *J. Appl. Cryst*., vol. 7, pp. 508–510, 1974, doi: 10.1107/S0021889874010302.

[137] C. F. Majkrzack, “Neutron diffraction studies of thin film multilayer structures,” *Physica B+C*, vol. 136, no. 1–3, pp. 69–74, 1986, doi: 10.1016/S0378-4363(86)80023-7.

[138] F. Mezei, and P. A. Dagleisch, “Corrigendum and first experimental evidence on neutron supermirrors,” *Commun. Phys*., vol. 2, pp. 41–43, 1977.

[139] J. B. Hayter, and H. A. Mook, “Discrete thin-film multilayer design for X-ray and neutron supermirrors,” *J. Appl. Cryst*., vol. 22, pp. 35–41, 1989, doi: 10.1107/S0021889888010003.

[140] E. Fermi, and W. H. Zinn, “Reflection of neutrons on mirrors,” *Phys. Rev*., vol. 70, p. 103, 1946.

[141] E. Fermi, and L. Marshall, “Interference phenomena of slow neutrons,” *Phys. Rev*., vol. 71, p. 666, 1947, doi: 10.1103/PhysRev.71.666.

[142] V.F. Sears, “Neutron scattering lengths and cross sections,” *Neutron News*, vol. 3, no. 3, pp. 26–37, 1992, doi: 10.1080/10448639208218770.

[143] G. P. Felcher, R. T. Kampwirth, K. E. Gray, and R. Felici, “Polarized-neutron reflections: A new technique used to measure the magnetic field penetration depth in superconducting niobium,” *Phys. Rev. Lett.*, vol. 52, p. 1539, 1984, doi: 10.1103/PhysRevLett.52.1539.

[144] V. K. Ignatovich, *The Physics of Ultra Cold Neutrons*. Oxford: UK: OUP, 1990.

[145] P. Croce, and B. Pardo, “Sur l’application des Couches Interferentielles a l’Optique des rayons X et de neutrons,” *Nouv. Rev. D’Optique Appliquee*, vol. 1, no. 4, pp. 229–232, 1970, doi: 10.1088/0029-4780/1/4/306.